Mass and radius constraints for neutron stars using the cooling tail method

Joonas Nättilä

Pro Gradu Thesis

Astronomy Division
Department of Physics
University of Oulu

Abstract

Neutron stars (NS) are the most compact objects that can be directly observed. They can be used to study properties of matter at supranuclear densities. This in turn gives us information to separate between numerous theoretical equations of states of dense matter. Thermonuclear (type-I) X-ray bursts from low mass X-ray binaries can be used to address this issue. Some of these bursts can be so energetic that they cause the whole photosphere of the NS to expand. The cooling of these photospheric radius expansion bursts can be compared to theoretical atmosphere models to obtain the mass and radius measurements of the NS. These measurements can then be used to differentiate between the different equations of state.

We present a set of differential equations needed to compute these atmospheric models. We introduce an exact treatment of Compton scattering via the relativistic integral equation and an angle-dependent redistribution function. Using these equations, we can construct a set of atmosphere models in plane-parallel approximation in a local thermodynamical equilibrium for hot NSs. The emergent spectra is then fitted by a diluted blackbody to obtain the dilution factor w and the colour-correction factor $f_{\rm c}$. On the other hand, the observed spectra from X-ray bursting neutron stars are close to thermal and can be fitted with a blackbody with two free parameters: the observed blackbody temperature $T_{\rm bb}$ and the normalization K. By equating the dilution factor w and the normalization K, we obtain a relation between the theoretical atmosphere models and the observations. This connection is the main idea of the so called cooling tail method. We then introduce a small correction to this method and discuss the consequences.

A common problem encountered using this method is that different bursts from a given system can yield completely different mass and radius measurements. This fact casts a doubt on the robustness of the entire method. We study the burst emission from 4U 1608–52 at various persistent fluxes. We find a strong dependence of the burst properties on the flux before the burst. Bursts that ignite during the hard state at a low accretion rate show

strong evolution of the apparent blackbody radius which is consistent with the model predictions of the neutron star atmosphere models. On the other hand, bursts occurring during the soft state at a higher accretion rate show constant apparent radius, which is inconsistent with the models.

We then use the hard state bursts only to constrain the neutron star mass and radius from our set of sources. By taking only the physically relevant results into account, we also get information of the chemical composition of the atmosphere. This then gives us a way to conclude if the atmosphere is hydrogen- or helium-rich. After we know the chemical composition, we constrain the NS radius to be between 12 and 16 km. This implies a stiff equation of state of neutron star matter.

Contents

Acknowledgements

First of all, I would like to thank Professor Juri Poutanen and Dr. Jari Kajava, my supervisors, for an extremely interesting topic and all the support. In addition, I wish to acknowledge the help provided by Dr. Valery Suleimanov. I would also like to extend my thanks to all the people in the astrophysics research group for the interesting discussions and support in general. Finally, I wish to thank my family, friends and especially Elizaveta for support and encouragement throughout my studies.

Chapter 1

X-ray bursts from neutron stars

1.1 Neutron stars

Neutron stars (NS) are one of the most exotic laboratories of the fundamental particle physics. They are extremely compact objects with typical radius of $R \approx 10$ km, mass M around $1.5 M_\odot$ and densities of about five to ten times the nuclear equilibrium density $\rho_0 \approx 2.7 \times 10^{14}$ g cm^{-3} (see e.g. Lattimer & Prakash 2001). Due to this, they seamlessly combine extreme phenomena of quantum mechanics and general relativity. Thus, they grant us a view of how the nature works in the ultimate frontier of our current knowledge.

General aspects of neutron stars, such as the mass and radius, are determined by the equations of hydrostatic equilibrium. The mathematical relation for a spherical object under hydrostatic equilibrium in general relativity is given by the so called Tolman-Oppenheimer-Volkov equations (Tolman, 1934; Oppenheimer & Volkoff, 1939)

$$\frac{dP}{dr} = -\frac{G[m(r) + 4\pi r^3 P/c^2](\rho + P/c^2)}{r[r - 2Gm(r)/c^2]} \tag{1.1}$$

and

$$\frac{dm(r)}{dr} = 4\pi\rho r^2, \tag{1.2}$$

where P and ρ are the pressure and density, $m(r)$ is the mass enclosed by a sphere of radius r, G is the gravitational constant and c is the speed of light in vacuum. For the solution of this equation, we need a relation between the pressure and the density $P = P(\rho)$ that we call the equation of state (EOS). These relations are commonly characterised by the compressibility of the matter and can be separated into three categories: soft, moderate and

stiff equations of state. After the EOS is known, we can obtain the mass and the radius of the neutron star. (Haensel et al., 2007).

The possible range of radii and masses obtained is restricted by the general relativistic Schwarzschild condition

$$R > \frac{2GM}{c^2}. \tag{1.3}$$

A similar, more strict constraint originates from the causality: the speed of sound in the matter can not be greater than the speed of light. This gives us the so called causality condition (Lattimer et al., 1990)

$$R \gtrsim 3\frac{GM}{c^2}. \tag{1.4}$$

From the observational point of view, the recent results from the accurately measured pulsar masses of around $2M_\odot$ (see e.g. Demorest et al. 2010; Antoniadis et al. 2013) give another constraint. According to theoretical calculations, the EOS needs to be rather stiff to support masses of this size. (Haensel et al., 2007).

Composition and structure

The interiors of the neutron star can be separated into 5 different regions: the atmosphere, the outer and inner crusts, and the outer and inner cores (see Figure 1.1). The atmosphere of the NS contain a negligible amount of mass but is important in shaping the emergent spectrum. The crust extends to about 1 to 2 km below the surface and is mainly composed of heavy nuclei. In the outer crust, the dominating nuclei is the iron ^{56}Fe with a typical density of around 10^6 g cm^{-3}. When moving inwards, closer to the core-crust interface, the density grows to around $\frac{1}{3}\rho_0$, and the nuclei start to have more and more neutrons in them. Deep in the crust, the atomic mass number can reach $A \sim 200$. When exceeding the neutron drip density $\rho_c = 4 \times 10^{11}$ g cm^{-3}, the neutrons start to leak out from the nuclei. Finally, when reaching the outer core, the matter becomes degenerate and consists of neutrons, protons, electrons and possibly muons. The composition of the inner core is unknown. According to different theories, hyperons or Bose condensates (pions or kaons) could appear in the mixture. Another possibility is that a transition to a mixed phase of hadronic and deconfined quark matter develops. The presence of these additional components could then soften the EOS considerably. (Lattimer & Prakash, 2001, 2004)

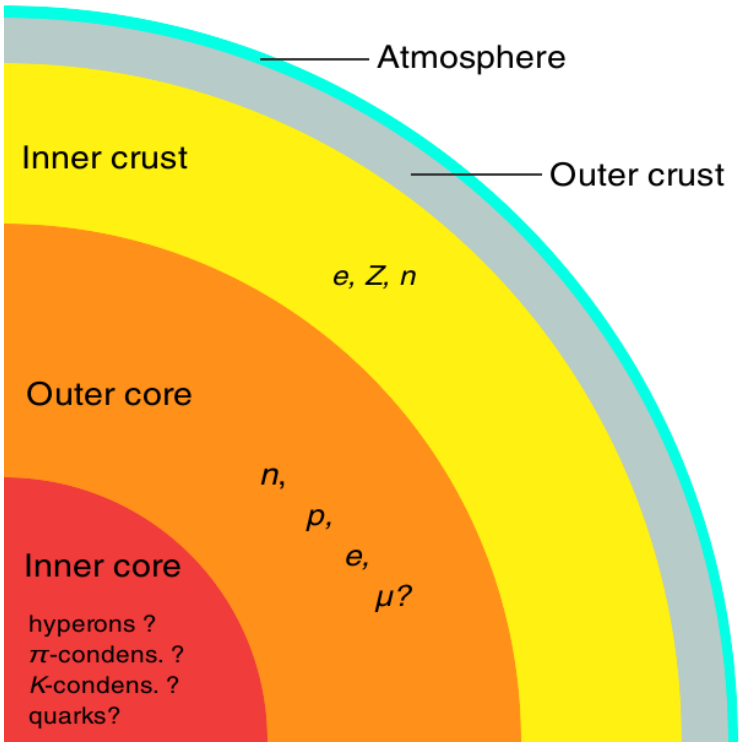

Figure 1.1: Neutron star structure.

One of the most important ongoing quests of astrophysics and nuclear physics is to measure the density of the NSs inner core. This would allow us to constrain the equation of state of the matter at supranuclear densities. However, theoretical studies of the matter at high densities have considerable uncertainties, largely because the conditions needed are unattainable in terrestrial laboratories. This, in turn, has led to many different theoretical predictions for the EOSs that all depend on the assumed composition of the core. By constraining the size of the neutron star from the observations, we would then be able to separate between different EOSs and, in the end, get information of the composition of the core. In this thesis, we propose to use the cooling of the so called thermonuclear bursts from the accreting neutron stars to measure the masses and the radii. Using these measurements, we can then set constraints on the EOS of dense matter.

1.2 History of X-ray flares

Before the X-ray bursts from neutron stars were even discovered, the idea of thermonuclear instability was proposed by Hansen & van Horn (1975). The bursts were first observed independently by Grindlay et al. (1976) and Belian et al. (1976). At first, these energetic X-ray flares were thought to originate from black hole systems inside globular clusters. The idea was, however, quickly disregarded as the location of the sources did not match locations of known globular clusters. There were also significant differences in the spectra of these sources compared to black holes (see e.g. van Paradijs 1978). Later on, a theory was proposed where the bursts originate in low mass X-ray binary systems (LMXB), where the main star is a compact neutron star and the companion is usually a smaller main sequence star, a white dwarf or a red giant. The confirmation for this idea came when the counterparts of Centaurus X–4 and Aql X–1 were observed to be dim late type stars (van Paradijs et al., 1980; Thorstensen et al., 1978) and the period of 1636–536 was measured to be about 3.8 hours (Pedersen et al., 1981). These observations were a proof that the bursts originate in the LMXB systems. The low period of 1636–536 was also taken as evidence for mass overflow from the smaller companion to the surface of the more massive neutron star (see Chap. 1.3). This can be seen as the beginning of the X-ray bursts research.

The real golden era of X-ray burst observations began in 1996 when NASA launched the Rossi X-ray Timing Explorer (*RXTE*). During this mission, numerous new X-ray sources were detected and our understanding of X-ray bursts was really tested. Currently over one hundred bursting X-ray sources are known (at the time of writing the exact number is 102 sources[1]).

1.3 Thermonuclear type-I bursts

Usually, the bursts have a rise time of about 1–10 seconds and a decay phase from 10 seconds to several minutes (see Figure 1.2). During this time, the neutron star releases around $10^{39} - 10^{40}$ ergs of energy. This energy comes from the unstable thermonuclear burning in the top layers of the neutron star. (Lewin et al., 1993; Strohmayer & Bildsten, 2006)

A fresh fuel for the burst is provided by the mass overflow from the companion star. This Roche lobe overflow happens when the companion exceeds the equipotential surface of the binary systems gravitational and

[1]http://www.sron.nl/ jeanz/bursterlist.html

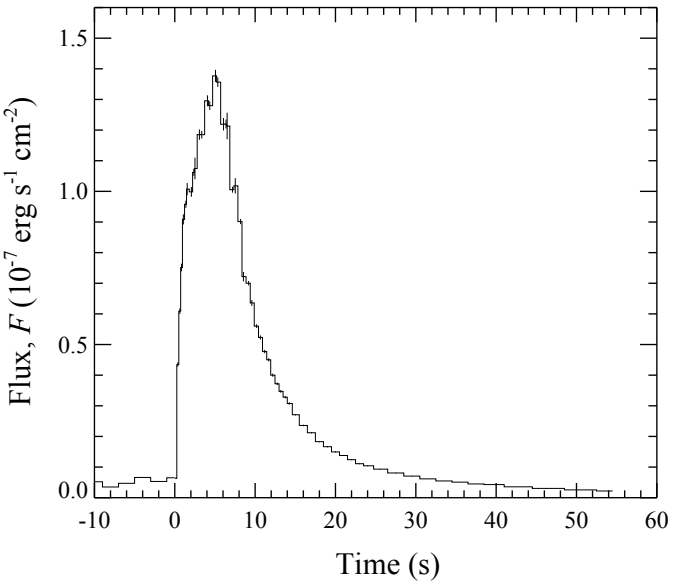

Figure 1.2: A light curve for burst observed from LMXB system 4U 1608–52.

centrifugal forces, known as Roche lobe. The material that resides outside of the companion star's Roche lobe begins to move towards the neutron star through the first Lagrangian point, L_1 (see figure 1.3). Because the system is rotating, the stream of gas from the companion does not directly hit the surface of the neutron star but begins to spiral in. Eventually, the gas flow intersects itself and forms a disc-like structure around the neutron star, called an accretion disc. Through this disc, the material then spirals onto the neutron star's surface. (Frank et al., 2002)

Eventually the new fresh fuel from the companion reaches the surface of the neutron star. As the mass transfer continues, the gas gets compressed and heated to such a high temperature and density that nuclear fusion is possible. This is the origin of the so called type-I burst, in which the fuel is being transferred to the surface during a time period that can range from hours to several days and eventually burned very rapidly with fusion reactions. On the other hand, type-II bursts originate from instabilities in the mass transfer if the flow of material is not constant. The most famous example of type-II bursting source is the Rapid Burster, found in 1976. All of the bursts analysed in this thesis are classified as type-I. (Lewin et al., 1993; Strohmayer & Bildsten, 2006)

Properties of the bursts are strongly affected by the chemical composition of the atmosphere and of the mass transfer rate per unit area $\dot{m} = \dot{M}/A_{\rm acc}$,

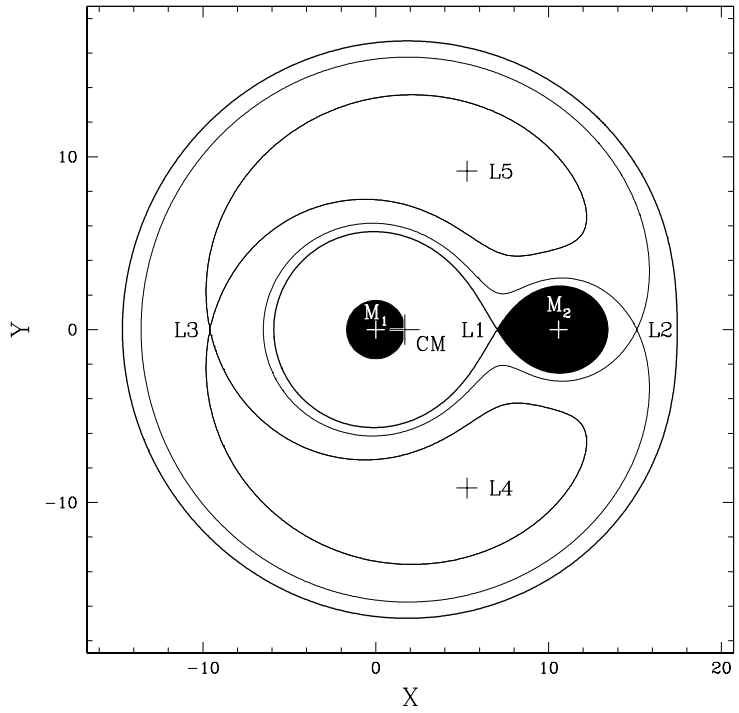

Figure 1.3: Two dimensional view of the Roche lobe of the binary system. The teardrop-shaped areas in the projection are the Roche lobes of the stars. Five Lagrangian points L_1, L_2, L_3, L_4 and L_5 are also shown. In these points, the forces between the two masses cancel each other. Through the saddle point L_1 the mass is transferred from the companion to the neutron star. Image courtesy of Carrier et al. (2003)

where $\dot{M}$ is the accretion rate and $A_{\rm acc}$ is the area covered by new material (usually taken to be the whole surface of the star which is about $A_{\rm acc} = 4\pi R^2 \approx 10^{13}$ cm^2 for radius of 10 km). The new accreted material is then burned via nuclear fusion reactions. In most cases, the temperature of the neutron star surface layers exceeds 10^7 K. In this case, the CNO-cycle is the dominant reaction. However, for a hotter temperature ($T > 8 \times 10^7$ K) the proton capture becomes more and more effective. At this temperature regime, hydrogen is burned via the hot CNO-cycle (Fowler & Hoyle, 1965)

$$^{12}C(p,\gamma)^{13}O\beta^{+14}N(p,\gamma)^{15}O(\beta^{+})^{15}N(p,\alpha)^{12}C.$$

Hydrogen continues to burn like this when

$$\dot{m} > 900 \text{ g cm}^{-2} \text{ s}^{-1} \times (Z_{\rm CNO}/0.01)^{1/2},$$

where Z_{CNO} is the relative mass of elements included in the CNO cycle compared to the whole mixture. With smaller mass transfer rates, the burning becomes unstable and hydrogen can ignite bursts where a mixture of hydrogen and helium is burned. For greater mass transfer rates of

$$\dot{m} > 2 \times 10^3 \text{ g cm}^{-2} \text{ s}^{-1} \times (Z_{\mathrm{CNO}}/0.01)^{13/18}$$

the atmosphere is so dense that helium can ignite before hydrogen is fully burned. In this case, we again have a mixture of hydrogen and helium burning, but the igniter is helium. In the regime between these two, it is possible to have pure helium burning which is followed by slower burning of hydrogen. Burning of pure helium is typically much more explosive because there are no weak interactions involved in the reactions. (Strohmayer & Bildsten, 2006)

In some cases, the radiation pressure force from the energy released in the burst can be even stronger than the gravitational force binding the outer layers of the star. In that case, the whole photosphere of the star expands momentarily (Tawara et al., 1984; Lewin et al., 1984). The luminosity corresponding to this limit is called the Eddington luminosity (see equation 3.18). After a while, the gravitation starts to dominate again and the photosphere collapses back to the surface. This moment is called the touchdown. It is the cooling phase after the touchdown of these photospheric radius expansion (PRE) bursts that we then use to measure the radius and the mass of the star.

Chapter 2

Data

2.1 Sources used in the analysis

LMXB systems can be divided into two classes, Z and atoll sources, depending on their timing properties and evolution of spectral colours (Hasinger & van der Klis, 1989). Difference between these two classes is that the Z sources tend to show quasi-periodic oscillations around $1 - 60$ Hz in their X-ray power spectrum while the atoll sources do not. The evolution of the spectral properties are also much faster in the Z sources, that can show changes in a timescale of days, whereas for the atoll sources $30 - 100$ days are needed. This separation into two different classes is thought to originate from a lower mass accretion rate in atoll sources (Muno et al., 2002). Due to a possible influence of this mass accretion on the burst properties, we hereafter focus only on the atoll sources. For our mass and radius analysis, we have selected all 12 atoll sources that have shown thermonuclear type-I bursts (see e.g. Galloway et al. 2008 for a catalogue of bursting X-ray sources and their properties). These sources are listed in Table 2.1.

For the mass and radius determination, we need the distance to the source to break the degeneracy of the corresponding equations (see Chapter 3.3.3). We obtain the distance estimates for these sources from the literature (see Table 2.1).

4U 1724–307 resides in a known globular cluster Terzan 2 and several distance estimates for this source have been made. To account for these, we adopt a similar distance distribution that was used by Suleimanov et al. (2011a). To take the different measurements into account, they choose a flat distribution of distances from 5.3 to 7.7 kpc with Gaussian tails of $1\sigma = 0.6$ kpc on both ends.

Table 2.1: Atoll LMXBs with type-I X-ray bursts

Source	RA	Dec	$P_{\rm orb}$ (hr)	Distance (kpc)
4U 1608–52	16 12 42.9	−52 25 22	...	5.8 ± 2.0
4U 1636–536	16 40 55.5	−53 45 05	3.8	6.0 ± 2.0
4U 1702–429	17 06 15.2	−43 02 09	...	5.5 ± 2.0
4U 1705–44	17 08 54.6	−44 06 02	...	5.8 ± 2.0
4U 1724–307	17 27 33.2	−30 48 07	...	$(5.3 - 7.7) \pm 0.6$
4U 1728–34	17 31 57.3	−33 50 03	...	5.2 ± 2.0
4U 1735–44	17 38 58.2	−44 27 00	4.65	8.5 ± 2.0
GX 3+1	17 47 56.0	−26 33 48	...	5.0 ± 2.0
4U 1746–37	17 50 12.6	−37 03 08	5.7	11.0 ± 0.9
3A 1820–303	18 23 40.5	−30 21 40	0.19	7.4 ± 0.4
Aql X-1	19 11 15.9	+00 35 06	19.0	3.9 ± 2.0
XTE J2123–058	21 23 16.1	−05 47 30	5.96	14.0 ± 2.0

4U 1746–37 is located in the globular cluster NGC 6441. We use a Gaussian distribution centred at 11.0 kpc with tails of $1\sigma = 0.9$ kpc as our distance estimate. Similar distance was used by Kuulkers et al. (2003).

3A 1820–303 is also known to reside in the globular cluster NGC 6624. Like previously, many distance estimates exist. To combine these, we use a Gaussian distribution of distances centred at 7.4 kpc with tails of $1\sigma = 0.7$ kpc, as was done by Kuulkers et al. (2003).

Most of the sources do not reside in any known globular cluster, making the distance to the source hard to measure. In these cases, we take a width Gaussian distribution of distances to cover all the possibilities with tails of $1\sigma = 2$ kpc. For the mean value, we choose the distance estimate made by Galloway et al. (2008) using the measurements of the peak Eddington flux. We would like to stress that this method should not be used as an exact distance measurement but only to show the approximate regime of distances that the source could reside in.

2.2 *RXTE* -mission

All of the data used in our analysis comes from the *Rossi X-ray Timing Experiment* -satellite (*RXTE*) (Bradt et al., 1993). On board the *RXTE* there are three instruments that cover the X-ray energies from about 2 to 200 keV. These are the Proportional Counter Array (PCA), All-Sky monitor (ASM) and High Energy X-ray Timing Experiment (HEXTE).

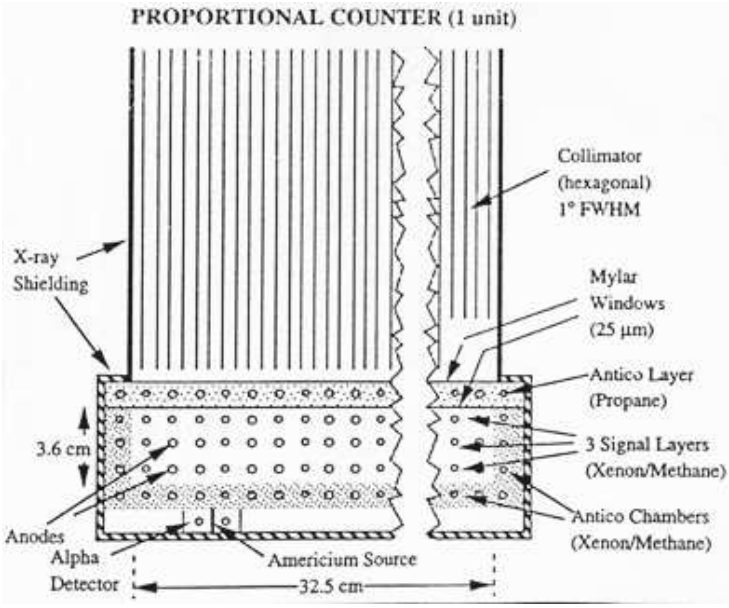

Figure 2.1: Schematic view of the PCA instrument. Image courtesy of Hale Bradt, NASA.

PCA (Jahoda et al., 2006) covers the low energy part from 2 to 60 keV. It consists of five separate proportional counter units (PCUs) with a total effective area of 6500 cm^2 (see figure 2.1). The PCUs work by utilising the photoelectric effect; the incoming X-ray photons remove electrons from the xenon atoms inside the units. These free electrons are then detected by the anodes as voltage pulses. The field of view is limited by a mechanical collimator into about one degree. Inside the PCU there is a propane filled veto volume on top of 3 layers of xenon cells, separated by an aluminised Mylar window. In addition to these, there is a separate xenon veto volume underneath. The amplification of the counters are being constantly monitored and calibrated by a radioactive americium sample, located in the bottom of the unit. Data is processed using up to six different Event Analyzers (EAs). Two of these are permanently set to so called Standard-1 data (0.125 s time resolution and one energy channel) and Standard-2 data (16 s time resolution and 129 energy channels). Third commonly used mode is the Event mode (time resolution down to 1μs and number of energy channels up to 256 are being used). All of the data used in this thesis comes from the PCA instrument.

ASM (Levine et al., 1996) consists of three scanning shadow cameras

sensitive in the energy range of 1.5 – 12 keV. It covers about 80% of the sky every 96 minutes.

HEXTE (Gruber et al., 1996) consists of two clusters of NaI/CsI scintillation detectors. It is used for the detection of high energy photons in the range 15–250 keV.

2.3 Data reduction

2.3.1 Observations and analysis

We analysed all publicly available data from the start of the *RXTE*-mission from 1995 December 30 to end of the mission, 2012 January 5. This data was obtained through the High Energy Astrophysics Science Archive Research Center[1] (HEASARC). For our analysis we have used the data from the PCA spectrometer of the *RXTE*. *RXTE*/PCA data were analysed with the help of the HEASOFT package (version 6.12) and response matrices were generated using the PCARSP (11.7.1) task of this package. To ensure consistent results with previously made analysis, we adapted a similar data reduction scheme as Galloway et al. (2008). In order to locate and identify the bursts, we extracted 1-s light curves from all available Standard-1 data from the sources, using the whole 2–60 keV energy range of the PCA. A mean count rate and a standard deviation were then computed for each observation. Those bins that exceeded the mean by more than 4σ deviations were then classified as burst candidates and visually inspected. Candidates were rejected if they showed attributes similar to other events that can produce sharp temporary peaks in count rates such as detector breakdowns or particle events.

2.3.2 Spectral analysis of individual bursts

Time resolved spectra for the burst candidates were extracted using initial integration time of 0.25, 0.5, 1.0 or 2.0 seconds depending on the peak count rate ($>$6000, $6000 - 3000$, $3000 - 1500$ or $<$1500 counts per second). Each time the count rate after the peak decreased by a factor of $\sqrt{2}$ the integration time was doubled to maintain approximately the same signal-to-noise ratio. A spectrum extracted from 16 s prior to the burst was subtracted as the background for each burst (see e.g. van Paradijs & Lewin 1987; Kuulkers et al. 2003). All the data was fitted using the XSPEC 12.8.0 package

[1] http://heasarc.gsfc.nasa.gov

(Arnaud, 1996) where the recommended systematic error of 0.5% was added when dealing with the PCA data (Jahoda et al., 2006). In order to take the low count rate bins into account, we also adopted Churazov weighting (Churazov et al., 1996). All error limits were obtained using the `error` task in XSPEC with one sigma confidence levels. The bolometric flux was estimated using the `cflux` model in the extended range of 0.01 – 200 keV.

These deadtime corrected spectra were then fitted with a blackbody model multiplied by interstellar absorption. We considered two models with an absorption column density of $N_{\rm H}$ free to vary as well as constant $N_{\rm H}$ fixed to the mean value over the burst. In the end, the mean constant value was chosen for the rest of the analysis. The best-fit parameters are the blackbody temperature $T_{\rm bb}$ and the normalization constant $K_{\rm bb} \equiv (R_{\rm bb}[{\rm km}]/D_{10})^2$, where $D_{10} = D/10$ kpc.

We also studied the choice of the model used by inspecting the $\chi^2/{\rm d.o.f} \equiv \chi^2_{\rm red}$ distributions (see Figure 2.2). In the case of the first burst from 4U 1724–307, it might be possible that our simple spectral model consisting of thermal radiation and background only is not enough, and a more complex model is required. We, however, keep this burst in our sample, for the sake of consistency, but warn the reader of the possible effects arising from this. Otherwise, our model fits follow the expected theoretical χ^2 distribution very well. Therefore, we conclude that our spectral model is acceptable.

2.3.3 Photospheric radius expansions

We examined the spectral variations of each burst. They were then classified according to the following criteria. Radius expansion was considered to have been occured when

1. the blackbody normalization $K_{\rm bb}$ reached a (local) maximum close to the peak of the burst,
2. the normalization begun to decrease after the peak and
3. the blackbody temperature $T_{\rm bb}$ reached a minimum at the same time as the $K_{\rm bb}$ reached a maximum.

With these criteria we found that around $10-60\%$ of the bursts were classified as showing radius expansion (see Table 2.2). As an exception, all 16 burst of 3A 1820-303 were classified as PRE bursts. On the other hand, we did not found any bursts from XTE J2123–058 that would fulfill the aforementioned criteria.

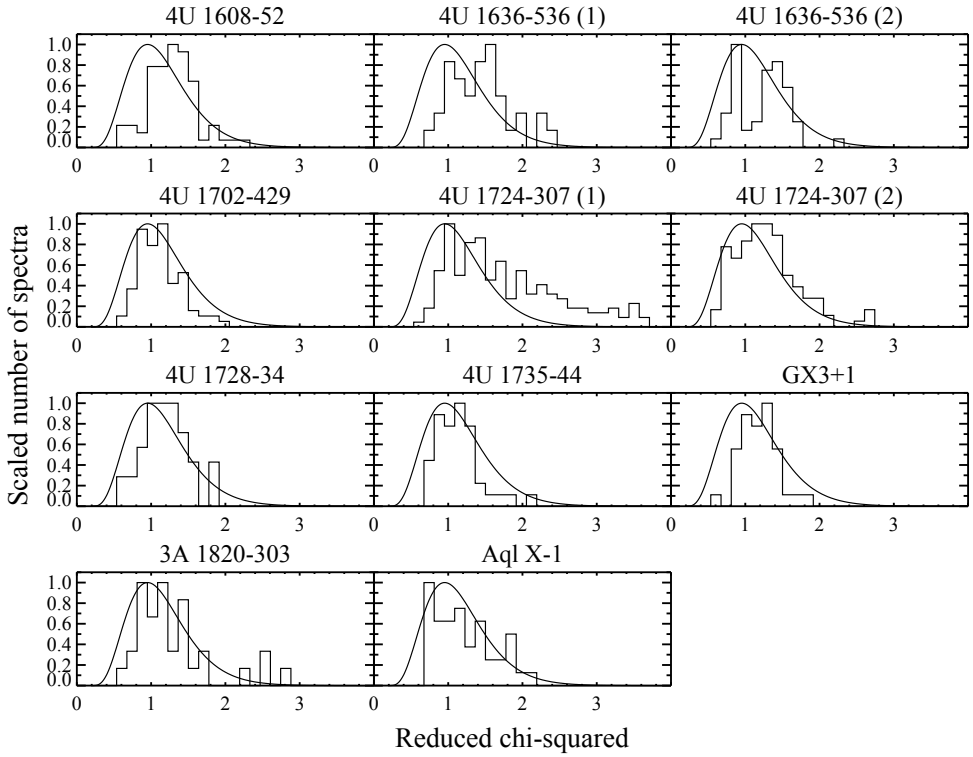

Figure 2.2: The histogram shows the reduced χ^2 distributions for the model fits of the PRE bursts from each source. The curve shows the theoretical χ^2 distribution. Notice that we have scaled our distributions to unity, for easier comparison. We have also separated the bursts from 4U 1636–536 and 4U 1724–307 into to two different samples that are later on derived in the Chapter 4.2.1.

As an example, Figure 2.3 shows a typical PRE burst from 4U 1608–52. This burst has a clear maximum of normalization $K_{\rm bb}$ after 3 seconds and a strong minimum around 8 seconds. These are all very strong indicators that the photosphere has extended and then collapsed back to the surface because the normalization is proportional to the size of the emitting surface. After the minimum, i.e. the touchdown point, the photosphere starts to cool down, as can be seen from the smoothly decreasing temperature. The time range enclosed between the two vertical lines corresponds to the important part of the cooling tail that we later use to measure the mass and radius of the star.

Table 2.2: Number of bursts

Source	$n^a_{\rm burst}$	$n^b_{\rm RE}$
4U 1608–52	47	21
4U 1636–536	362	84
4U 1702–429	49	7
4U 1705–44	83	8
4U 1724–307	4	4
4U 1728–34	128	94
4U 1735–44	22	13
GX 3+1	3	2
4U 1746–37	13	3
3A 1820–303	16	16
Aql X-1	70	14
XTE J2123–058	4	0

[a] Number of type-I thermonuclear bursts.
[b] Number of bursts exhibiting photospheric radius expansion.

2.3.4 Characterising persistent emission

To get additional information of the state of the source prior to each PRE burst, we also studied the persistent emission. The persistent flux level prior to the burst was calculated using 160 s long deadtime corrected spectra. The backgrounds of the PCA detectors were estimated with the `CM_bright_VLE` model. These spectra were then fitted with a model consisting of blackbody (`bbodyrad`) and powerlaw (`powerlaw`) components attenuated by interstellar absorption (`phabs`) over the range 2.5–25 keV. The detected source flux was estimated using the `flux` task of XSPEC.

In order to characterise the persistent spectrum, we also computed hard and soft X-ray colours as the ratio of flux in the $(8.6-18.0)/(5.0-8.6)$ keV and $(3.6-5.0)/(2.2-3.6)$ keV energy bands. From these colour ratios we were able to define the $S_{\rm Z}$ coordinate locus using a similar method as in Galloway et al. (2008). First, the aforementioned colour ratios were calculated for every public observation that were sliced into 160s long pieces. Several points were then selected to define the basic shape of the curve. From these, we constructed a smooth curve using a spline interpolation. A value of $S_{\rm Z}=1.0$ was then assigned to the upper-right corner of the Z-shape and $S_{\rm Z}=2.0$ to the lower-left corner. The unit arc-length was defined as a distance between these two points. The value of $S_{\rm Z}$ for any given point was calculated by finding the nearest point on the curve and finding the value of the arc-length

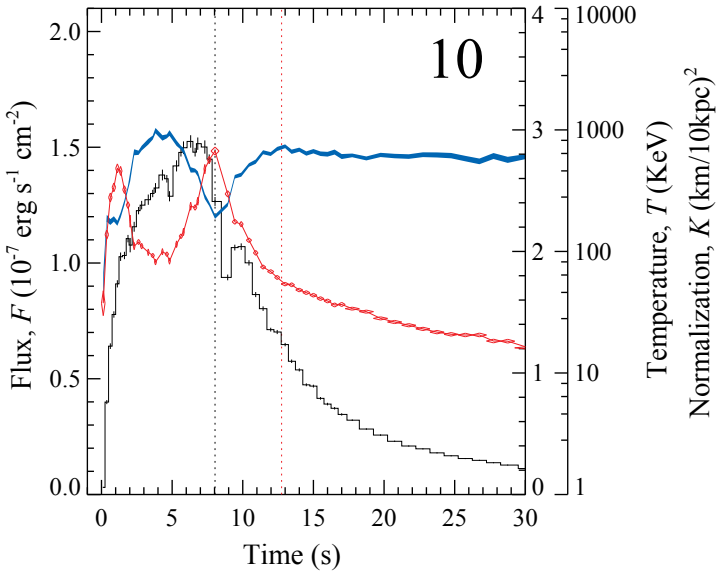

Figure 2.3: A typical PRE burst from 4U 1608–52. The black line shows the estimated bolometric flux (left-hand y-axis) in units of 10^{-7} erg cm^{-2} s^{-1}. The blue ribbon shows the 1σ limits of the normalization (outer right-hand y-axis) in $(\mathrm{km}/\mathrm{D}_{10\mathrm{kpc}})^2$. The red line show the blackbody temperature (inner right-hand y-axis) in keV. The black vertical dashed line marks the time of touchdown and the red vertical dashed line the moment when the flux has decreased to half of the touchdown flux.

S_Z there. For 4U 1608–52 this is explictly done as an example and the spline curve is shown in Figure 2.4.

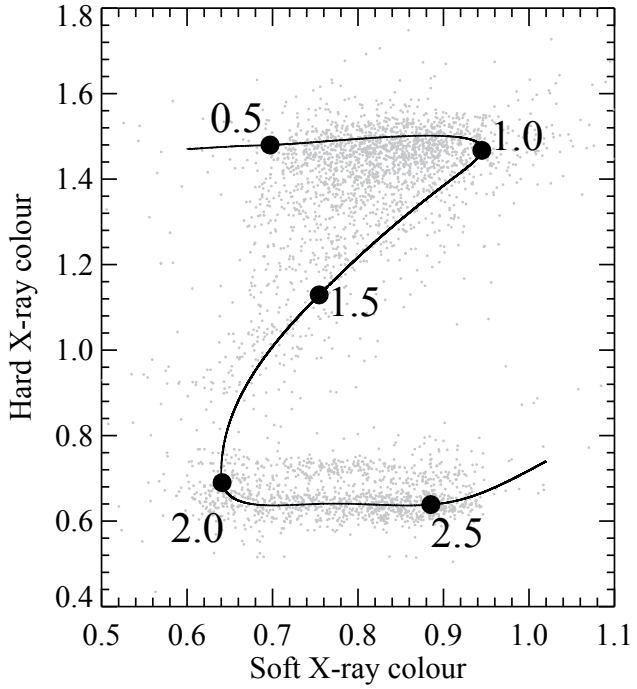

Figure 2.4: Colour-colour diagram for 4U 1608–52. The spline curve and corresponding S_Z values are shown on top of colour-values calculated from all of the publicly available data.

Chapter 3

Theory of atmosphere models

The cooling of neutron star atmospheres after X-ray bursts can be used to constrain neutron star masses and radii. This is done by comparing the cooling of the observed PRE bursts and theoretical models. Here we derive a connection between the observations and models and also present a basic framework for the calculation of neutron star atmospheres. We follow the methods of Suleimanov et al. (2012) who computed hot X-ray bursting neutron star atmospheres in hydrostatic equilibrium on plane-parallel approximation.

3.1 Method of computation

Hydrostatic equilibrium

The structure of the atmosphere model is described by a set of differential equations. The first one is the hydrostatic equilibrium equation

$$\frac{\mathrm{d}P_{\mathrm{g}}}{\mathrm{d}m} = g - g_{\mathrm{rad}}, \tag{3.1}$$

where P_{g} is gas pressure, g_{rad} is the radiative acceleration and column density m is found from

$$\mathrm{d}m = -\rho \mathrm{d}z, \tag{3.2}$$

where ρ is the gas density and z the vertical distance. Surface gravity g of the star is

$$g = \frac{GM}{R^2}(1+z), \tag{3.3}$$

where

$$1 + z = (1 - R_{\mathrm{S}}/R)^{-1/2} \tag{3.4}$$

is the redshift factor and $R_{\rm S} = 2GM/c^2$ is the Schwarzschild radius of the neutron star.

Radiative transfer

The second equation needed is the radiative transfer equation. In plane-parallel approximation it can be formulated using a specific intensity $I(x, \mu)$ and a source function $S(x, \mu)$ as

$$\mu \frac{{\rm d}I(x,\mu)}{{\rm d}\tau(x,\mu)} = I(x,\mu) - S(x,\mu), \tag{3.5}$$

where $\mu = \cos\theta$ is the cosine between the angles of the surface normal and the direction of propagation. The dimensionless photon energy $x = h\nu/m_{\rm e}c^2$ is given in the units of electron rest mass where h is the Planck constant, ν is the photon frequency and $m_{\rm e}$ is the electron rest mass. Change in the optical depth can also be related to the opacities and the column density m by

$${\rm d}\tau(x,\mu) = [\sigma(x,\mu) + k(x,\mu)]{\rm d}m, \tag{3.6}$$

where $k(x, \mu)$ is the opacity per unit mass due to free-free and bound-free transitions and $\sigma(x, \mu)$ is the electron scattering opacity.

Compton scattering kernel

For the exact electron scattering opacity, a few additional equations are needed. In the work done by Suleimanov et al. (2012), they introduced an exact angle-dependent relativistic Compton scattering redistribution function (RF) (Aharonian & Atoyan, 1981; Prasad et al., 1986; Nagirner & Poutanen, 1994; Poutanen & Svensson, 1996) in order to compute the electron scatering opacity accounting for induced scattering. This can be formulated using the aforementioned RF $R(x, \mu; x_1, \mu_1)$ that describes the probability that a photon with a dimensionless energy x propagating in a direction μ is scattered to an energy x_1 and to a direction μ_1. The electron scattering opacity is then

$$\sigma(x,\mu) = \kappa_{\rm e}\frac{1}{x}\int_0^\infty x_1{\rm d}x_1 \int_{-1}^{1} {\rm d}\mu_1 R(x_1,\mu_1;x,\mu)\left(1 + \frac{CI(x_1,\mu_1)}{x_1^3}\right), \tag{3.7}$$

where Thomson scattering opacity is

$$\kappa_{\rm e} = \sigma_{\rm T}\frac{N_{\rm e}}{\rho} \approx 0.2(1+X)\ {\rm cm}^2\ {\rm g}^{-1}, \tag{3.8}$$

and σ_{T} is the Thomson cross-section, N_{e} is the electron number density and X is the hydrogen mass fraction. C is a constant defined as

$$C = \frac{1}{2m_{\mathrm{e}}} \left(\frac{h}{m_{\mathrm{e}}c^2} \right)^3 . \tag{3.9}$$

Source function

The source function, present in the radiative transfer equation (3.5), is a sum of the thermal part and the scattering part

$$S(x,\mu) = \frac{k(x)}{\sigma(x,\mu)+k(x)} B_x + \frac{\kappa_{\mathrm{e}}}{\sigma(x,\mu)+k(x)} \tag{3.10}$$

$$\times \left(1 + \frac{CI(x,\mu)}{x^3} \right) x^2 \int_0^\infty \frac{\mathrm{d}x_1}{x_1^2} \int_{-1}^{+1} \mathrm{d}\mu_1 R(x,\mu;x_1,\mu_1) I(x_1,\mu_1),$$

where the dimensionless Planck function B_x can be formulated using the normal frequency related Planck function B_ν by

$$B_x = B_\nu \frac{\mathrm{d}\nu}{\mathrm{d}x} = \frac{x^3}{C} \frac{1}{\exp(x/\Theta)-1}, \tag{3.11}$$

where the temperature T can be presented as the dimensionless electron temperature as

$$\Theta = \frac{kT}{m_{\mathrm{e}}c^2}, \tag{3.12}$$

where k is the Boltzmann constant.

Radiation pressure acceleration

The radiation pressure acceleration present in equation (3.1) is then expressed using the RF as

$$g_{\mathrm{rad}} = \frac{\mathrm{d}P_{\mathrm{rad}}}{\mathrm{d}m} = \frac{2\pi}{c} \frac{\mathrm{d}}{\mathrm{d}m} \int_0^\infty \mathrm{d}x \int_{-1}^{+1} \mu^2 I(x,\mu) \mathrm{d}\mu \tag{3.13}$$

$$= \frac{2\pi}{c} \int_0^\infty \mathrm{d}x \int_{-1}^{+1} [\sigma(x,\mu)+k(x)][I(x,\mu)-S(x,\mu)] \mu \mathrm{d}\mu,$$

where the derivative with respect to m is replaced by the first moment of the radiation transfer equation (3.5).

Energy balance and equation of state

The third and fourth main equations are the energy balance equation

$$\int_0^\infty \int_{-1}^{+1} [\sigma(x,\mu) + k(x)][I(x,\mu) - S(x,\mu)]\mathrm{d}\mu = 0 \tag{3.14}$$

and the ideal gas law

$$P_\mathrm{g} = N_\mathrm{tot} kT, \tag{3.15}$$

where N_tot is the number density of all particles. In addition equations for particle and charge conservations are needed.

Number densities of elements

Finally, in order to calculate the number densities of all ionisation and excitation states of elements, we can assume a local thermodynamic equilibrium (LTE). Using this approximation, number densities can be obtained from familiar Boltzmann and Saha equations. Effects from the pressure ionisation for hydrogen and helium populations can be additionally taken into account using the occupation probability formalism (Hummer & Mihalas, 1988) as described by Hubeny et al. (1994).

3.2 Colour-correction factors

In order to get theoretical relations for the cooling of the bursts, we can compute the atmosphere models for various temperatures from the aforementioned set of equations. The initial temperature can be taken as low as necessary and the computations are then continued until $g_\mathrm{rad}/g = 1$, that corresponds to the Eddington limit. All computed emergent spectra can be fitted by the diluted blackbody spectrum (Suleimanov et al., 2011b)

$$F_\mathrm{E} \approx w B_\mathrm{E}(f_\mathrm{c} T_\mathrm{eff}), \tag{3.16}$$

where w is the dilution factor, f_c is the colour-correction factor and T_eff is the effective temperature. This effective temperature corresponds to a temperature for which a blackbody would radiate the same total amount of energy that our system would. Hence, it is the temperature of a source that would emit an equal amount of energy as we observe, but by thermal radiation only. At high luminosities the dilution factor w is close to $1/f_\mathrm{c}^4$.

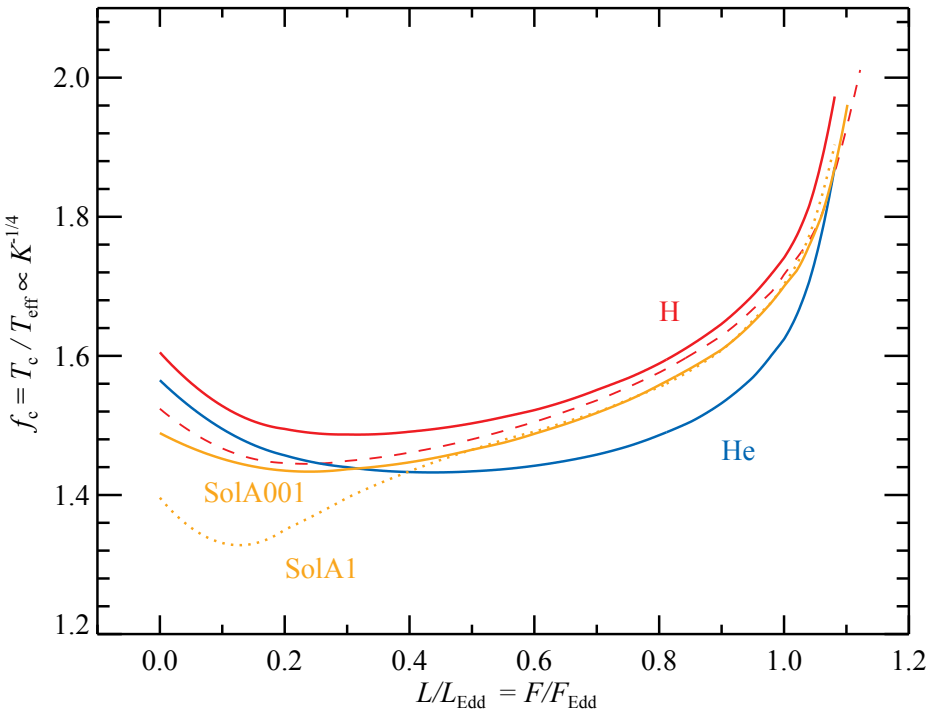

Figure 3.1: Theoretical evolutions of the colour correction factor against the luminosity for pure hydrogen (red), pure helium (blue) and the solar ratio of H/He and the subsolar metal abundance of $Z = 0.01 Z_\odot$ (orange, SolA001) are shown for a surface gravity of $\log g = 14.0$. The dotted orange curve corresponds to a solar ratio of H/He and a solar abundance of heavy elements (SolA1). For comparison, colour-correction computed for $\log g = 14.6$ is shown for a pure hydrogen composition (red, dashed line).

Technically this fitting procedure is done in the energy band $(3-20)\times(1+z)$ keV corresponding to the observed range of the *RXTE*/PCA detector.

From this we get the theoretical evolution of the colour correction factor against the luminosity for different chemical compositions and surface gravities (see Figure 3.1)

The first big difference between different cooling tracks is between pure hydrogen and pure helium. It is caused by the fact that at the first approximation the colour correction factor is related to the ratio between the temperature of the upper layers of the atmosphere and the effective temperature $T_{\rm eff}$. This leads to smaller f_c values for pure helium atmospheres because cooling is more effective when helium is present.

Another feature is the dip at the low luminosities for atmospheres that have heavy elements. At low luminosities, iron is not completely ionised, leading to an absorption edge at 9 keV due to bound-free transitions from the ground levels of the H-like Fe XXVI ion ($E_{\rm ion} = 9.278$ keV) and He-like Fe XXV ion ($E_{\rm in} = 8.828$ keV). This edge reduces the number of hard X-ray photons leading to a softer spectrum and a smaller colour-correction factor. On the other hand, at high luminosities iron is completely ionised, so no edge is seen.

3.3 Cooling tail method

Neutron star mass and radius can be constrained from the information in the cooling tail as was shown by Suleimanov et al. (2011a) (see also Suleimanov et al. (2011b, 2012)). Here we follow those steps and derive a connection between the observations and the theoretical atmosphere models of the neutron stars. We also introduce a small correction to this method and discuss the consequences.

3.3.1 Basic relations

First, we present some relations between observed and real physical NS parameters. Due to the light bending and gravitational redshift the luminosity L_∞, effective temperature $T_{\rm eff,\infty}$ and the apparent neutron star radius R_∞ observed by a distant observer differ from the luminosity L, the effective temperature $T_{\rm eff}$, and the circumferential radius R, measured at the surface of the neutron star, by the following relations (Lewin et al., 1993):

$$L_\infty = \frac{L}{(1+z)^2}, \quad T_{\rm eff,\infty} = \frac{T_{\rm eff}}{1+z}, \quad R_\infty = R(1+z). \tag{3.17}$$

These then affect the Eddington luminosity

$$L_{\rm Edd} = \frac{4\pi GMc}{\kappa_{\rm e}}(1+z) = 4\pi R^2 \sigma_{\rm SB} T_{\rm Edd}^4, \tag{3.18}$$

where $\sigma_{\rm SB}$ is the Stefan-Boltzmann constant and $T_{\rm Edd}$ is the effective temperature corresponding to Eddington luminosity defined for Thomson scattering opacity. The observed Eddington luminosity is then

$$L_{\rm Edd,\infty} = \frac{4\pi GMc}{\kappa_{\rm e}} \frac{1}{1+z} \tag{3.19}$$

and the observed Eddington flux

$$F_{\rm Edd} = \frac{L_{\rm Edd,\infty}}{4\pi D^2} = \frac{GMc}{\kappa_{\rm e} D^2} \frac{1}{1+z}. \tag{3.20}$$

Finally, from these equations we get the Eddington temperature for the distant observer

$$T_{\rm Edd,\infty} = \frac{T_{\rm Edd}}{1+z} = \left(\frac{gc}{\sigma_{\rm SB}\kappa_{\rm e}}\right)^{1/4} \frac{1}{1+z} = \left(\frac{F_{\rm Edd}}{\sigma_{\rm SB}}\right)^{1/4} \left(\frac{R_\infty}{D}\right)^{-1/2}. \tag{3.21}$$

3.3.2 Atmosphere models and observations

Neutron star emergent spectra at high luminosities are close to the diluted blackbody spectra due to strong energy exhange between high-energy photons and relatively cold electrons at the NS surface layers

$$\mathcal{F}_E \approx w B_E(f_{\rm c} T_{\rm eff}). \tag{3.22}$$

The energy integrated (i.e. bolometric) total flux is then

$$\mathcal{F} = \int_0^\infty \mathcal{F}_E dE \approx \int_0^\infty w B_E(f_{\rm c} T_{\rm eff}) dE = w f_{\rm c}^4 \sigma_{\rm SB} T_{\rm eff}^4. \tag{3.23}$$

These spectral properties are confirmed by numerous computations of X-ray bursting neutron star atmospheres (London et al., 1984, 1986; Ebisuzaki, 1987; Madej, 1991; Pavlov et al., 1991; Zavlin & Shibanov, 1991; Zavlin et al., 1996; Suleimanov & Poutanen, 2006; Suleimanov et al., 2011b, 2012). At high luminosities the dilution factor w is close to $1/f_{\rm c}^4$ so we can approximate the emergent energy integrated spectra by

$$w f_{\rm c}^4 \sigma_{\rm SB} T_{\rm eff}^4 \approx \sigma_{\rm SB} T_{\rm eff}^4. \tag{3.24}$$

Using the basic neutron star parameters (Lewin et al., 1993) and equation (3.24), the bolometric flux observed by a distant observer is

$$\mathcal{F}_\infty = \mathcal{F} \frac{R^2}{D^2} \frac{1}{(1+z)^2} \approx \sigma_{\rm SB} T_{\rm eff}^4 \frac{R^2}{D^2} \frac{1}{(1+z)^2}. \tag{3.25}$$

On the other hand, the observed spectra from X-ray bursting neutron stars are close to thermal and can be fitted with a blackbody with two free

parameters: the observed blackbody temperature $T_{\rm bb}$ and the normalization $K = (R_{\rm bb}\ [\rm km]/D_{10})^2$. The observed flux is

$$F_{E,\infty} = B_E(T_{\rm bb})\frac{R_{\rm bb}^2}{D^2} \tag{3.26}$$

and the energy integrated (i.e. bolometric) flux observed by a distant observer is

$$F_\infty = \sigma_{\rm SB} T_{\rm bb}^4 \frac{R_{\rm bb}^2}{D^2} = \sigma_{\rm SB}\left(\frac{f_{\rm c} T_{\rm eff}}{1+z}\right)^4 \frac{R_{\rm bb}^2}{D^2}, \tag{3.27}$$

where we have used the relations

$$T_{\rm bb} = f_{\rm c} T_{\rm eff,\infty} = f_{\rm c}\frac{T_{\rm eff}}{1+z} \tag{3.28}$$

between temperatures. After this we can find a relation between normalization and the NS radius from equations (3.25) and (3.27):

$$\frac{R_{\rm bb}^2}{D^2} = \frac{R^2}{D^2}\frac{(1+z)^2}{f_{\rm c}^4} = \frac{R_\infty^2}{D^2}\frac{1}{f_{\rm c}^4}, \tag{3.29}$$

where $R_\infty = R(1+z)$ is the apparent NS radius at infinity. These can be further transformed into a relation between the colour correction factor and the normalization (Penninx et al., 1989; van Paradijs et al., 1990)

$$K^{-1/4} = f_{\rm c} A, \tag{3.30}$$

where

$$A = \left(\frac{R_\infty\ [\rm km]}{D_{10}}\right)^{-1/2} = \left(\frac{(1+z)R\ [\rm km]}{D_{10}}\right)^{-1/2} \tag{3.31}$$

is a constant. This relation is the key idea behind the cooling tail method. It combines the theoretical and observational values together, because the evolution of the normalization K at sub-Eddington luminosities reflects the evolution of the dilution factor w. Due to the connection between w and $f_{\rm c}$, the evolution of K then also gives us information of the crucial colour correction factor.

This method can be sligthly corrected by not using the approximate relation $w \approx f_{\rm c}^{-4}$ but by directly using equation (3.23). New observed energy integrated flux is then

$$\mathcal{F}_\infty = \frac{w f_{\rm c}^4 \sigma_{\rm SB} T_{\rm eff}^4}{(1+z)^4}\frac{R^2(1+z)^2}{D^2}. \tag{3.32}$$

This gives us a small correction to the observed bolometric flux because of the additional factor wf_c^4. From this we can derive a new connection between different radii:

$$R_{bb}^2 = wR^2(1+z)^2 = wR_\infty^2 \tag{3.33}$$

and expressing this through K and A we have

$$K = wA^{-4} = w\left(\frac{R_\infty\ [\mathrm{km}]}{D_{10}}\right)^2. \tag{3.34}$$

This means that the evolution of $K^{-1/4} - F_{bb}$ must not be related to the previously used theoretical relation $f_c - l(\equiv L/L_{Edd})$, but to $w^{-1/4} - wf_c^4 l$. This introduces a small correction that is negligible near the Eddington limit but changes the evolution slightly at lower luminosities.

3.3.3 Touchdown method: mass and radius

In an ideal situation the burst is observed from a passively cooling atmosphere. This enables us to derive the mass and the radius for the neutron star using the Eddington flux (3.20), if we assume that the moment the Eddington limit is reached coincides with the touchdown. Using the compactness $u = R_S/R = 1 - (1+z)^{-2}$ we get

$$R = \frac{2\kappa_e D^2 F_{Edd}}{c^3} u^{-1}(1-u)^{-1/2} \tag{3.35}$$

$$= 14.138\ (1+X) D_{10}^2 F_{Edd} u^{-1}(1-u)^{-1/2} \times 10^7\ \mathrm{km}, \tag{3.36}$$

and for the mass

$$\frac{M}{M_\odot} = \frac{R}{2.95\ \mathrm{km}} u. \tag{3.37}$$

On the other hand, if we know the colour-correction factor f_c at the end of the cooling process (usually this is taken to be between about $1.4 - 1.6$), we get a second constraint for the mass and radius using equation (3.30). The radius is then

$$R = R_\infty\sqrt{1-u} = D_{10}^2 A^{-2}\sqrt{1-u}\ \mathrm{km}, \tag{3.38}$$

and the mass is solved using the previous equation (3.37). Finally, from the Eddington temperature (3.21) we get the (third distance independent) relation for radius

$$R = \frac{c^3}{2\kappa_e \sigma_{SB} T_{Edd,\infty}^4} u(1-u)^{3/2}, \tag{3.39}$$

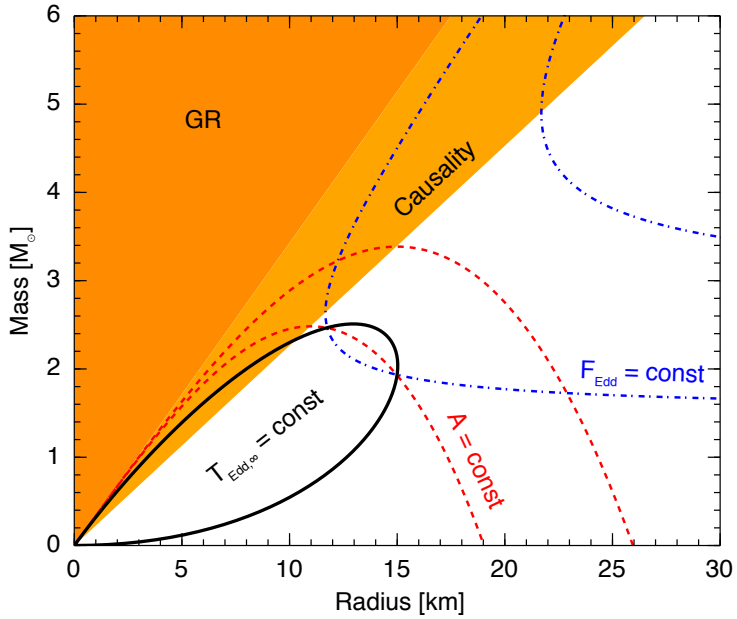

Figure 3.2: The mass and radius constraints from the observed values. The black solid curve corresponds to constraints from the constant Eddington temperature for a distant observer $T_{\mathrm{Edd},\infty}$, given by equation (3.39). The red dashed curve is for a constant Eddington flux F_{Edd} given by equation (3.35). The blue dot-dashed curve gives constraints for $A = \mathrm{const}$ from equation (3.38). Mass is always found from equation (3.37). The upper left region is excluded by the constraints from the general relativity (dark orange) and causality (light orange). If the distance is too large, curves of constant F_{Edd} and A do not cross; in this case, no solution exists.

and the mass is again solved like previously. All three of these curves (equations 3.35, 3.38 and 3.39) then cross each other at one or two points (see Figure 3.2), if the equation

$$u(1-u) = 14.138(1+X)D_{10}F_{\mathrm{Edd}}A^2 \times 10^7 \tag{3.40}$$

has a real-valued solution for u. This happens if $u(1-u) < 1/4$ and it can be translated into an upper limit of the distance of

$$D_{10} \leq \frac{0.0177}{(1+X)A^2 F_{\mathrm{Edd},-7}}. \tag{3.41}$$

In the opposite case, there is no physical solution for the mass and radius for the given observables.

3.3.4 Cooling tail method

To escape the needs of initial conditions for the values of the colour-correction factor at the end of cooling and the selection of a fixed point for the Eddington limit, we can use the information from the whole cooling tail. Because normalization derived from the data is related to the dilution factor w and the flux is related to the luminosity, we can fit the observed cooling track by the theoretical evolution. This removes the need to choose these values arbitarily. We call this the cooling tail method in contrast to previously described touchdown method.

In many cases, the bursts are well described by the theoretical curves. This is especially true for the high luminosity part where we observe striking similarities between the shape of the dilution factor and the data. In many cases, the data is also explained down to very low luminosities, but in these regions we need to be careful as heating from the mass flow can influence the cooling. In the next chapter, we address this issue more carefully and derive a result that only the so called hard state bursts should be used with this method.

Chapter 4

Hard and soft state bursts

A common problem encountered using the touchdown method is that different bursts from a given system can yield completely different mass and radius measurements. This fact casts a doubt on the robustness of the entire method. In this chapter, we study the PRE burst emission from 4U 1608–52 at various persistent fluxes to address this issue (see Latvala 2012 for a study of other sources too).

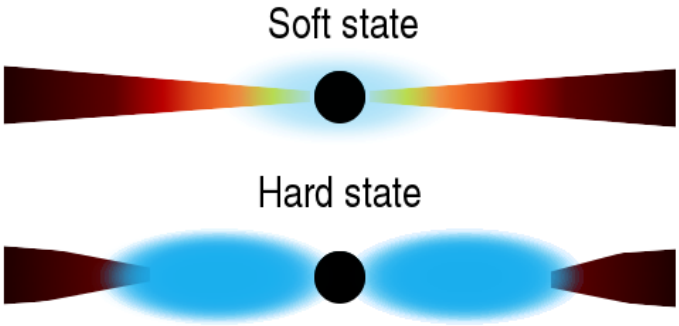

Figure 4.1: Accretion disc geometry in the soft and the hard state. In the soft state, the disc extends near the NS and matter is transferred directly. In the hard state, the disc is, on the contrary, truncated and the matter is transferred through a hot inner flow (blue).

By inspecting the sources with different luminosities, we also end up observing them in different spectral states. These states are called the hard (island) and the soft (banana) state (see Figure 4.1). While the accretion rate is small (low persistent flux), the disc is thought to be truncated and the inner edge is far away from the neutron star. This is called the hard state.

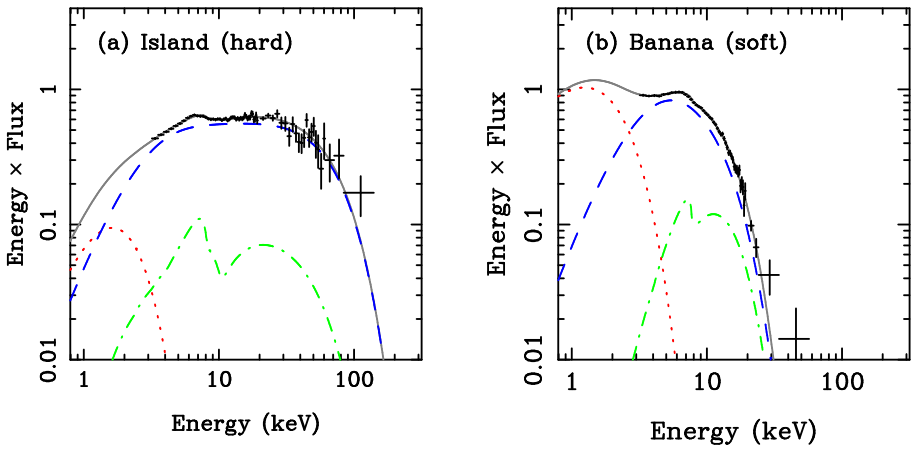

Figure 4.2: Two spectral states of 4U 1705–44. The so called island state (hard state) (a) is fitted by a blackbody (dotted), its thermal Comptonization (dashed) and the reflection component (dot-dashed). The so called banana state (soft state) (b) is fitted by a disc blackbody (dotted), the thermal Comptonization of unseen hot seed photons (dashed) and the reflection component (dot-dashed). Image courtesy of Done et al. (2007)

In this case, the matter is transferred through a hot, optically thin inner flow. The spectrum is dominated by a thermal Comptonization component from the optically thin gas surrounding the NS (see figure 4.2a). When the accretion rate increases (high persistent flux), the truncation radius of the disc is thought to decrease and the hot inner flow to collapse into an optically thick disc. This marks the change from the hard state into the soft state. The spectrum is then dominated by the radiation from the standard disc and a boundary layer (see figure 4.2b). (Gilfanov et al., 1999, 2003).

4.1 PRE burst properties

The time-resolved spectral parameters of the analysed PRE bursts from 4U 1608–52 are shown in Figure 4.3. These bursts show typical characteristics of photospheric radius expansion: fast rise of the flux at the beginning and peak in the normalization after a few seconds. The temperature evolution of these bursts also shows the characteristic double peaked structure from the heating and cooling of the surface when the photosphere expands and then collapses.

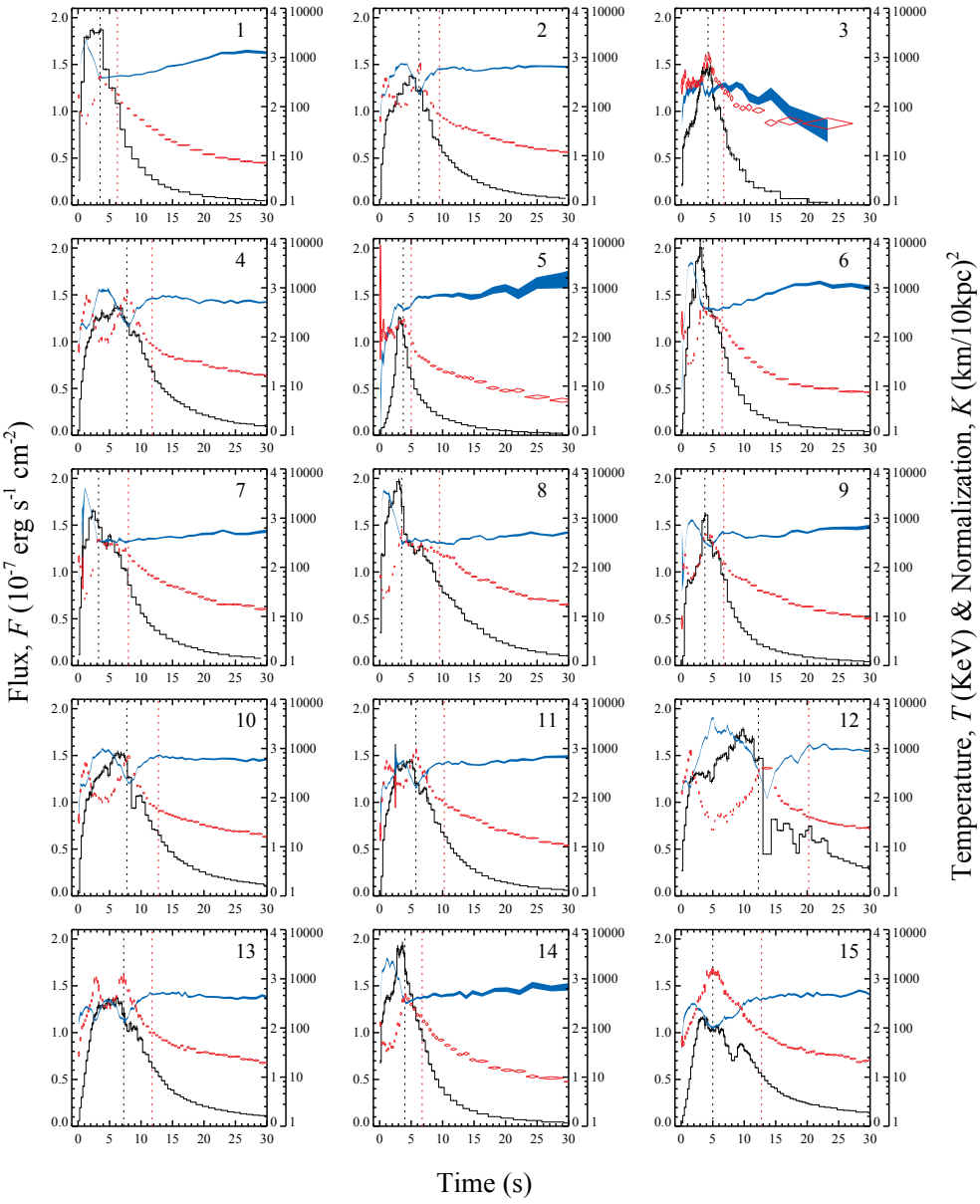

Figure 4.3: Flux, temperature and blackbody radius evolutions during the PRE bursts of 4U 1608–52. The black line in each panel shows the estimated bolometric flux (left-hand y-axis) in units of 10^{-7} erg cm^{-2} s^{-1}. The blue ribbon shows the 1σ limits of the normalization (outer right-hand y-axis) in $(\mathrm{km/D_{10kpc}})^2$. The red diamonds show the 1σ errors for blackbody temperature (inner right-hand y-axis) in keV.

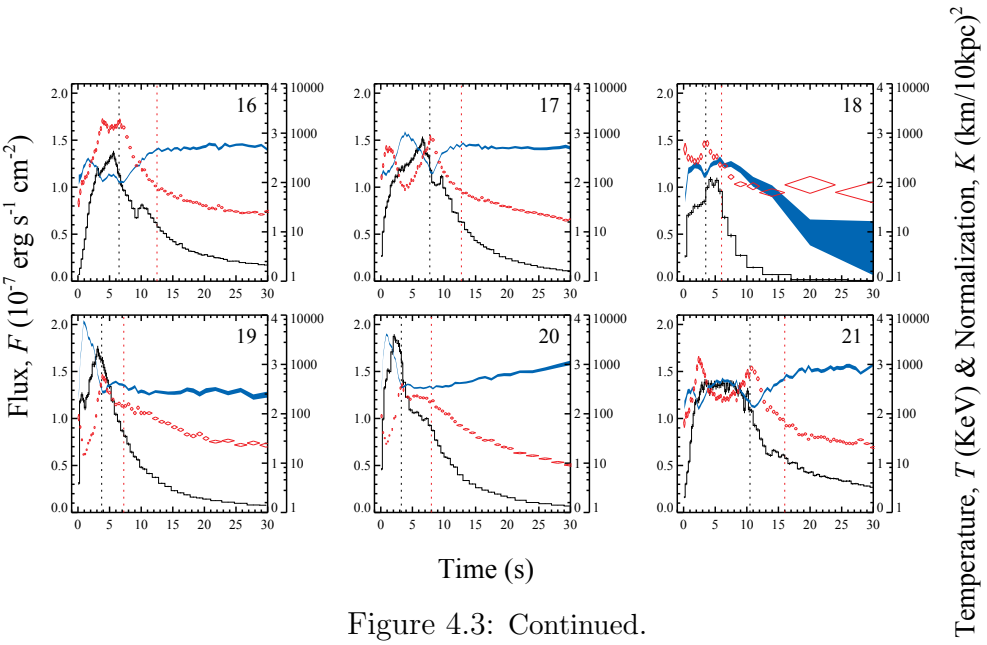

Figure 4.3: Continued.

We compare the cooling of these PRE bursts to theoretical models of neutron star atmospheres (see Chapter 3 for full description of the cooling tail method). Because the models do not take external heating from accreting matter into account, the cooldown must be due to a passively cooling neutron star atmosphere. For a passively cooling atmosphere the models predict that the colour-correction factors fall from $f_{\rm c} \approx 1.8$ at the touchdown when $L \approx L_{\rm Edd}$ to about $f_{\rm c} \approx 1.4$ at $L \approx 0.5 L_{\rm Edd}$ (Suleimanov et al., 2011b, 2012). This means that the ratio of the blackbody normalizations at the same luminosities can be used as an indicator of whether the burst follows the theoretical $K^{-1/4} \propto f_{\rm c}$ dependency. For K_1 at luminosity $L \approx L_{\rm Edd}$ and K_2 at $L \approx 0.5 L_{\rm Edd}$ the ratio is $K_2/K_1 \approx 3.5$. This is an important reference value, that we use to discriminate between different bursts.

4.2 Observed hard and soft state

When analyzing different bursts, we indeed found a clear dependency between the K_2/K_1 ratio and the persistent flux prior to the bursts (Figure 4.4a) as the persistent emission depends on accretion rate. This can also be seen with other model-independent parameters (Table 4.1) derived from the bursts (Figure 4.4b-d). The bursts can now be separated into two distinct groups. The first group contains bursts 2, 4, 10, 11, 12, 13, 15, 16, 17 and 21 that occur at low persistent fluxes and have K_2/K_1 ratios similar to that predicted by the atmosphere models. The second group, on the other hand, has bursts 1, 3, 5, 6, 7, 8, 9, 14, 18, 19 and 20 with smaller K_2/K_1 ratios and higher persistent fluxes. This behaviour can be understood as accretion flow influencing the cooling. At low accretion rates (low persistent flux), the flow can be disrupted by the burst for the duration of the cooling, whereas at higher accretion rates (high persistent flux), the flow is continuous and strong enough to influence the cooling atmosphere. The same way as with K_2/K_1 ratios, we can divide the bursts based on the shape of the spectrum of the persistent emission prior to the bursts (see Figure 4.5). Bursts that occur at high persistent fluxes are in the soft state, in which they are dominated by thermal radiation in the soft X-rays. At a low accretion rate, the spectrum of the persistent emission of the bursts, on the other hand, is qualitatively more flat. These hard states are dominated by the Compton tail that increases the emission in the hard X-rays relative to the soft part of the spectrum.

The persistent emission can also be characterised by the S_Z parameter. The S_Z is thought to be proportional to the mass accretion rate but the exact calibration is not known (Vrtilek et al., 1990). We calculate the S_Z parameter locus for each burst, corresponding to the soft and hard X-ray colours (see Figure 4.6). The division between the two states can be also seen here. The hard state bursts are located at values of $S_Z < 2$ whereas the soft state bursts all have $S_Z > 2$.

After dividing the bursts based on the persistent flux, it is clear that at low persistent fluxes the evolution of bursts is consistent with the models. The temperature evolution of every hard state burst seems to trace a common cooling track whereas the soft state bursts follow many different separate tracks (see Figure 4.7). The same trend can be seen in the $F - K^{-1/4}$ plane: all hard state bursts follow the atmosphere model very well while the soft state bursts have almost constant normalization K throughout the whole range of luminosities. Therefore, we propose that only the hard state bursts should be used when constraining masses and radii of neutron stars.

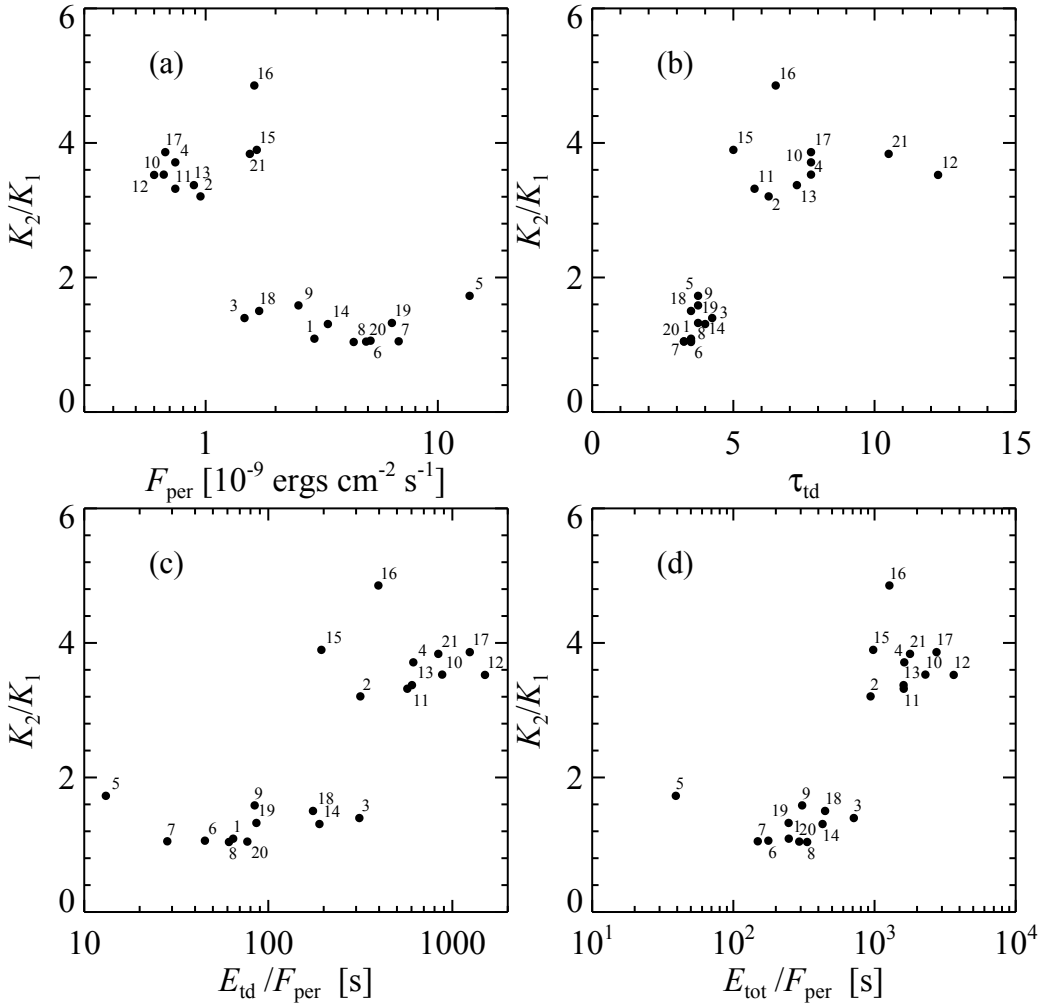

Figure 4.4: Ratio of blackbody normalizations in the touchdown and at 1/2 of the touchdown flux as a function of the (a) persistent flux before the burst, (b) time between the start of the burst and the touchdown, (c) ratio of the fluence emitted until touchdown and the persistent flux, and (d) the ratio of the total burst fluence to the persistent flux. Notice that the second group of bursts is located around $K_2/K_1 \approx 3.5$, as predicted by the atmosphere models.

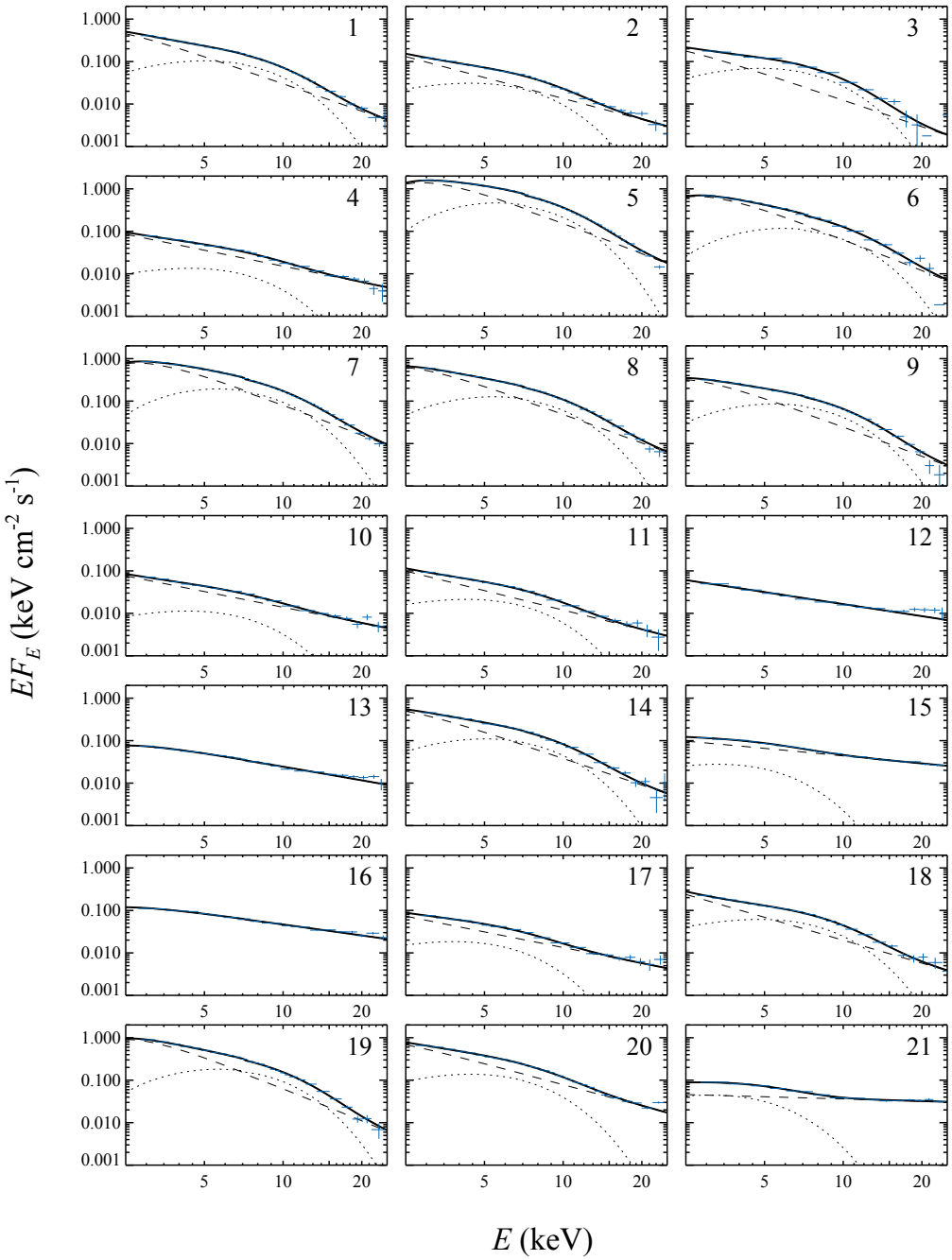

Figure 4.5: The spectrum of the persistent emission of 4U 1608–52 prior to each PRE burst. The model (black line) shown is a blackbody (dotted line) plus a powerlaw (dashed line) attenuated by an interstellar absorption over the data points with corresponding errors (blue crosses).

Table 4.1: Photospheric radius expansion X-ray bursts from 4U 1652–08

#[a]	ID[b]	Start time[c]	$F^{d}_{\rm peak,-9}$	$E^{e}_{\rm burst,-6}$	$E^{f}_{\rm td,-6}$	$\tau^{g}_{\rm td}$	$F^{h}_{\rm per,-9}$	$S^{i}_{\rm Z}$
1	30062-01-01-00	50899.58773	187 ± 3	0.73 ± 0.01	0.189 ± 0.002	3.50 ± 0.38	2.94 ± 0.03	2.04 ± 0.03
2	30062-01-02-05	50914.27536	138 ± 3	0.89 ± 0.01	0.300 ± 0.002	6.25 ± 0.13	0.94 ± 0.02	1.98 ± 0.03
3	50052-02-01-01	51612.03154	147 ± 5	1.03 ± 0.02	0.459 ± 0.005	4.25 ± 0.13	1.47 ± 0.04	2.22 ± 0.11
4	50052-01-04-00	51614.07195	136 ± 4	1.20 ± 0.01	0.454 ± 0.002	7.75 ± 0.25	0.74 ± 0.02	1.47 ± 0.07
5	70059-01-08-00	52499.40469	125 ± 3	0.54 ± 0.01	0.180 ± 0.002	3.75 ± 0.13	13.74 ± 0.05	2.56 ± 0.03
6	70059-01-20-00	52524.10226	200 ± 11	0.91 ± 0.01	0.232 ± 0.002	3.50 ± 0.13	5.13 ± 0.09	2.20 ± 0.06
7	70059-01-21-00	52526.16075	165 ± 3	1.01 ± 0.01	0.192 ± 0.002	3.25 ± 0.38	6.79 ± 0.03	2.27 ± 0.04
8	70059-03-01-00	52529.18003	197 ± 4	1.45 ± 0.01	0.265 ± 0.002	3.50 ± 0.25	4.34 ± 0.04	2.06 ± 0.04
9	70058-01-39-00	52536.31899	161 ± 3	0.77 ± 0.01	0.212 ± 0.002	3.75 ± 0.38	2.51 ± 0.03	2.15 ± 0.03
10	70069-01-01-00	52542.50148	153 ± 4	1.52 ± 0.01	0.627 ± 0.003	7.75 ± 0.50	0.66 ± 0.02	1.71 ± 0.07
11	70059-01-26-00	52546.90013	144 ± 3	1.19 ± 0.01	0.421 ± 0.003	5.75 ± 0.13	0.74 ± 0.02	1.94 ± 0.05
12	80406-01-04-08	52727.18595	178 ± 4	2.18 ± 0.01	0.902 ± 0.003	12.25 ± 0.25	0.60 ± 0.02	0.68 ± 0.38
13	90408-01-04-04	53104.40863	137 ± 3	1.43 ± 0.01	0.537 ± 0.003	7.25 ± 0.13	0.89 ± 0.02	1.37 ± 0.08
14	93408-01-23-02	54434.97404	193 ± 5	1.44 ± 0.01	0.637 ± 0.004	4.00 ± 0.13	3.36 ± 0.05	2.24 ± 0.04
15	93408-01-25-06	54452.11616	116 ± 3	1.62 ± 0.01	0.323 ± 0.002	5.00 ± 0.13	1.66 ± 0.02	0.82 ± 0.06
16	93408-01-26-04	54461.03122	136 ± 4	2.06 ± 0.01	0.642 ± 0.004	6.50 ± 0.13	1.62 ± 0.02	0.82 ± 0.07
17	93408-01-59-03	54692.07527	151 ± 4	1.84 ± 0.01	0.833 ± 0.004	7.75 ± 0.13	0.67 ± 0.02	1.76 ± 0.10
18	94401-01-25-02	54997.68005	108 ± 4	0.76 ± 0.02	0.297 ± 0.005	3.50 ± 0.25	1.70 ± 0.03	1.99 ± 0.10
19	95334-01-03-08	55270.22087	174 ± 5	1.56 ± 0.02	0.546 ± 0.004	3.75 ± 0.13	6.34 ± 0.05	2.10 ± 0.06
20	96423-01-11-01	55725.15573	187 ± 3	1.44 ± 0.01	0.378 ± 0.003	3.25 ± 0.13	4.91 ± 0.04	2.20 ± 0.04
21	96423-01-35-00	55890.37128	139 ± 5	2.76 ± 0.02	1.300 ± 0.006	10.50 ± 0.25	1.55 ± 0.04	0.85 ± 0.09

[a] Burst number. [b] The observation ID during which the burst was observed. [c] The burst start time in MJD. [d] The peak flux, in units of 10^{-9} erg cm^{-2} s^{-1}. [e] The burst fluence, in units of 10^{-6} erg cm^{-2} . [f] The burst fluence until the touchdown, in units of 10^{-6} erg cm^{-2} . [g] Time from the beginning of the burst to the touchdown (s). [h] The persistent flux level prior to the burst (2.5–25 keV, units of 10^{-9} erg cm^{-2} s^{-1}). [i] Position $S_{\rm Z}$ on the colour-colour diagram.

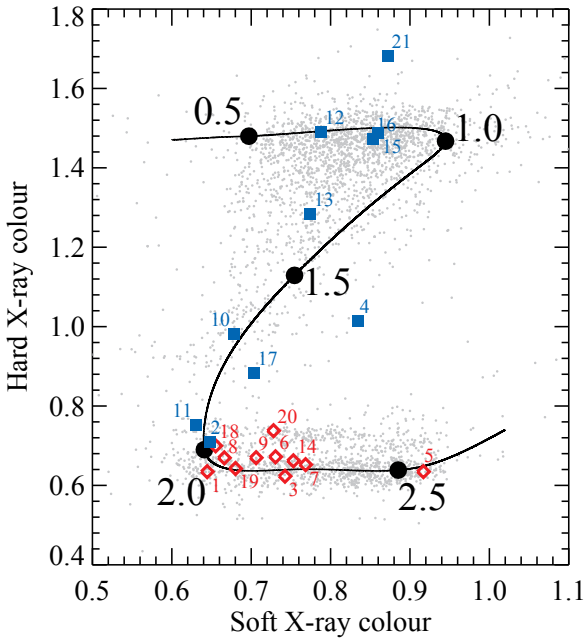

Figure 4.6: Colour-colour -diagram for 4U 1608–52 showing the S_Z parameter locus before each burst. The hard state bursts are marked with blue squares and soft state bursts with red diamonds.

4.2.1 Constructing cooling tails

In order to exclude the external heating, we now expand the work done in this chapter to cover the other sources (see Chapter 2.1) as well. Our aim is to construct one cooling tail for each source from the hard state bursts only. First, the cooling tail of each PRE burst is visually inspected. Then the hard state bursts are selected from the colour-colour diagrams (see Figure 4.8) according to the following criteria

- Only the bursts with a colour-colour parameter $S_Z \lesssim 2.0$ are considered, implying a small accretion rate to the surface of the star.
- The ratio of the normalizations K_1 at the touchdown and K_2 at half of the touchdown flux must be over 1.5.
- The cooling tail of the burst needs to show sufficiently smooth evolution similar to the theoretical models in the $F - K^{-1/4}$ plane.

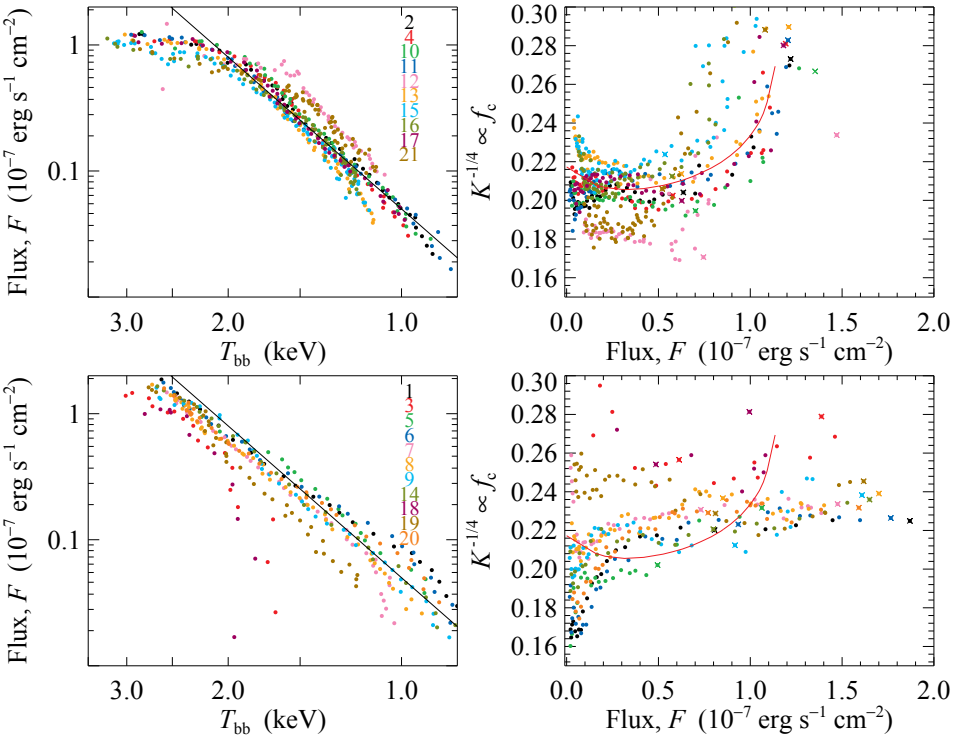

Figure 4.7: X-ray burst evolution for the hard state (upper panels) and the soft state (lower panels) bursts. The cooling tracks for the different bursts are shown from the touchdown to the end of the burst. In the left panels the black line corresponds to a powerlaw with an index of 4. In the right panels, the pure hydrogen atmosphere model is shown with a red line.

A combined cooling tail for each source is then constructed (see Table 4.2 for statistics) from the bursts fulfilling the aforementioned criteria.

For 4U 1636–536 and 4U 1724–307 we found two separate groups of different cooling tracks that traced a slightly different paths in the $F - K^{-1/4}$ plane. In these cases, we used both tracks separately. The other track is always indicating a smaller Eddington flux and a larger colour-correction factor (i.e. smaller normalization) in the tail. The origin of this effect is still unknown.

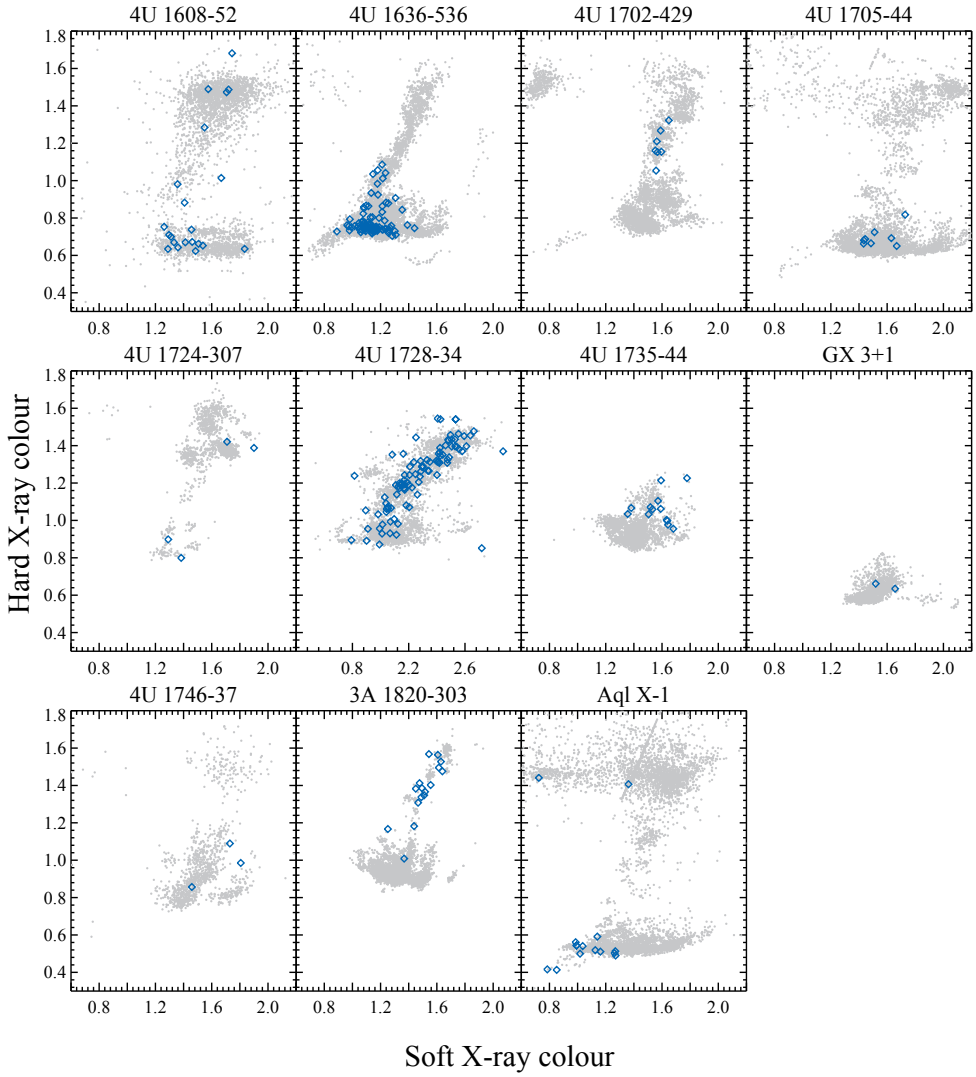

Figure 4.8: Colour-colour diagrams for the sources used. The blue open diamonds show S_Z locus prior each PRE burst.

Table 4.2: Number of bursts

Source	$n^a_{\rm burst}$	$n^b_{\rm RE}$	$n^c_{\rm HRE}$
4U 1608–52	47	21	6
4U 1636–536	362	84	3+5
4U 1702–429	49	7	7
4U 1705–44	83	8	0
4U 1724–307	4	4	1+1
4U 1728–34	128	94	68
4U 1735–44	22	13	1
GX 3+1	3	2	0
4U 1746–37	13	3	1[d]
3A 1820–303	16	16	16
Aql X-1	70	14	2
XTE J2123–058	4	0	0

[a] Number of type-I thermonuclear bursts.
[b] Number of bursts exhibiting photospheric radius expansion
[c] Number of hard state radius expansion bursts.
[d] This burst was omitted from a later use due to having only 3 data points.

Chapter 5

Mass and radius constraints

We fit the dependence of the normalization constant $K^{-1/4}$ on the observed flux F by the theoretical curves $w^{-1/4} - w f_c^4 l (\equiv L/L_{\rm Edd})$ computed for 2 chemical compositions (hydrogen and helium) and three surface gravities ($\log\, g = 14.0$, 14.3 and 14.6). We obtain two best fit parameters, $A = (R_\infty[\mathrm{km}]/D_{10})^{-1/2}$ and $F_{\rm Edd}$. For surface gravity, the best value is chosen by considering all of the values and then choosing the one giving the best correspondence with the mass and radius results.

Data from the touchdown to half of the $F_{\rm Edd}$ is used. First half of the cooling tail is preferred because at low luminosities it is possible that the accretion flow influences the cooling, causing deviations from theoretical models. In addition, the evolution of the colour correction is strongest near the Eddington flux. Before fitting the models, a systematic error of around $0.5 - 2\%$ is added to $K^{-1/4}$ values so that $\chi^2_{\rm red}$ values of around 1 are attained from the model fits. The uncertainties in A and $F_{\rm Edd}$ are obtained with a bootstrap method.

After obtaining the colour correction f_c by fitting the theoretical models, the observed temperature $T_{\rm bb}$ is transformed to the effective temperature observed by a distant observer $T_{\rm eff,\infty}$ by dividing with f_c according to the previously presented relations

$$T_{\rm bb} = f_c \frac{T_{\rm eff}}{(1+z)} = f_c T_{\rm eff,\infty}. \tag{5.1}$$

The corresponding value of colour correction is obtained by finding the closest point from the theoretical curve $L/L_{\rm Edd} - f_c$ for each point separately in the $F - K^{-1/4}$ plane. After this correction, we confirm that the cooling goes according to the $L \propto T_{\rm eff}^4$ relation (see the second column of Figure 5.1).

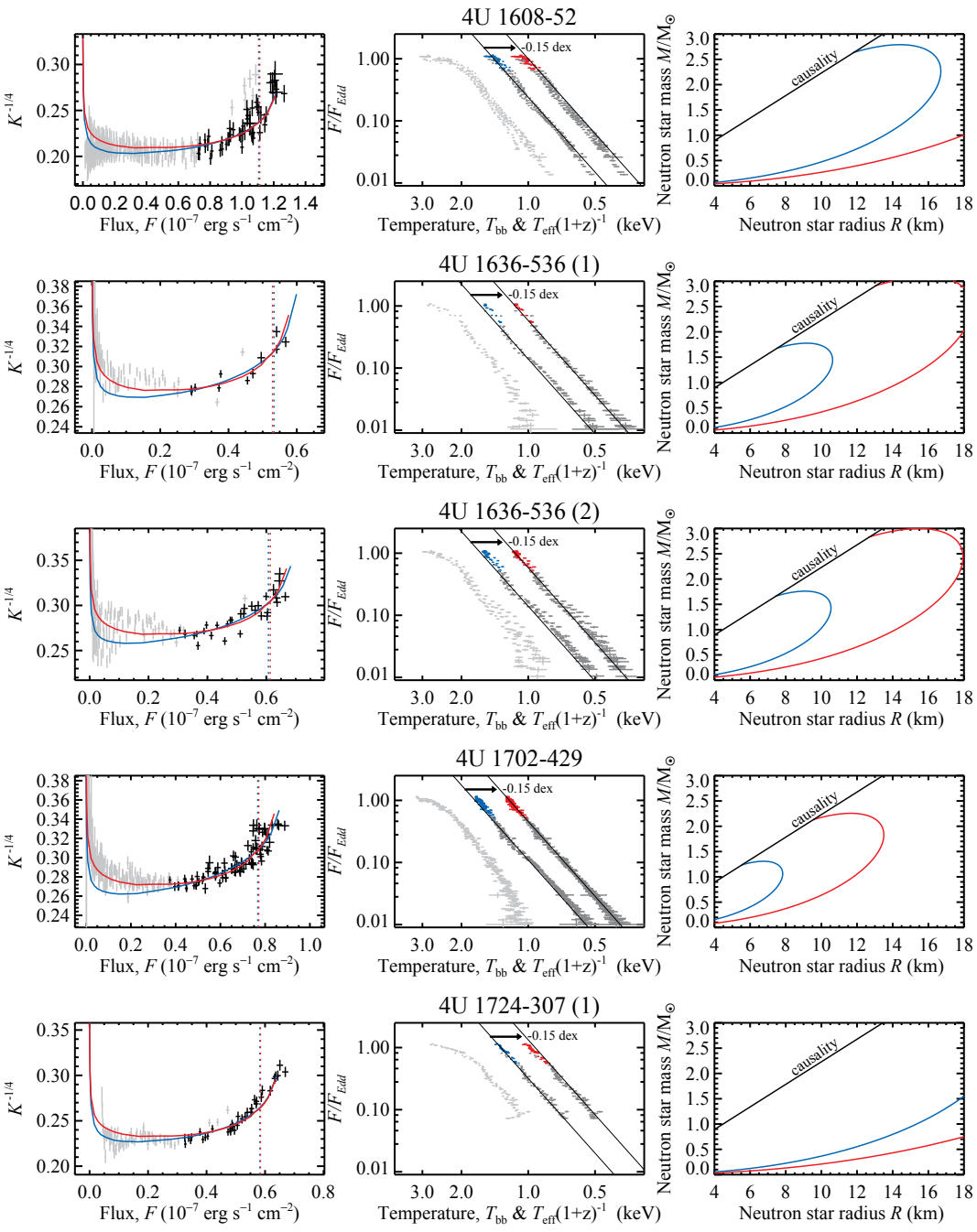

Figure 5.1: Normalization $K^{-1/4}$ ($\propto f_c$) vs. Flux F are presented for each source in the first column of figures. Curves show the theoretical cooling tail relation for hydrogen (blue) and helium (red) atmosphere models. Vertical dashed lines show the Eddington flux for both models. In the second column of figures, the blackbody temperature T_{bb} is shown for each cooling tail with grey crosses. The blue (hydrogen) and the red (helium) crosses show the colour-corrected temperatures $T_{eff}(1+z)^{-1}$ for both models. Dark grey points show the low-luminosity end of the cooling tail, not used in the fitting. (Continued on the next page.)

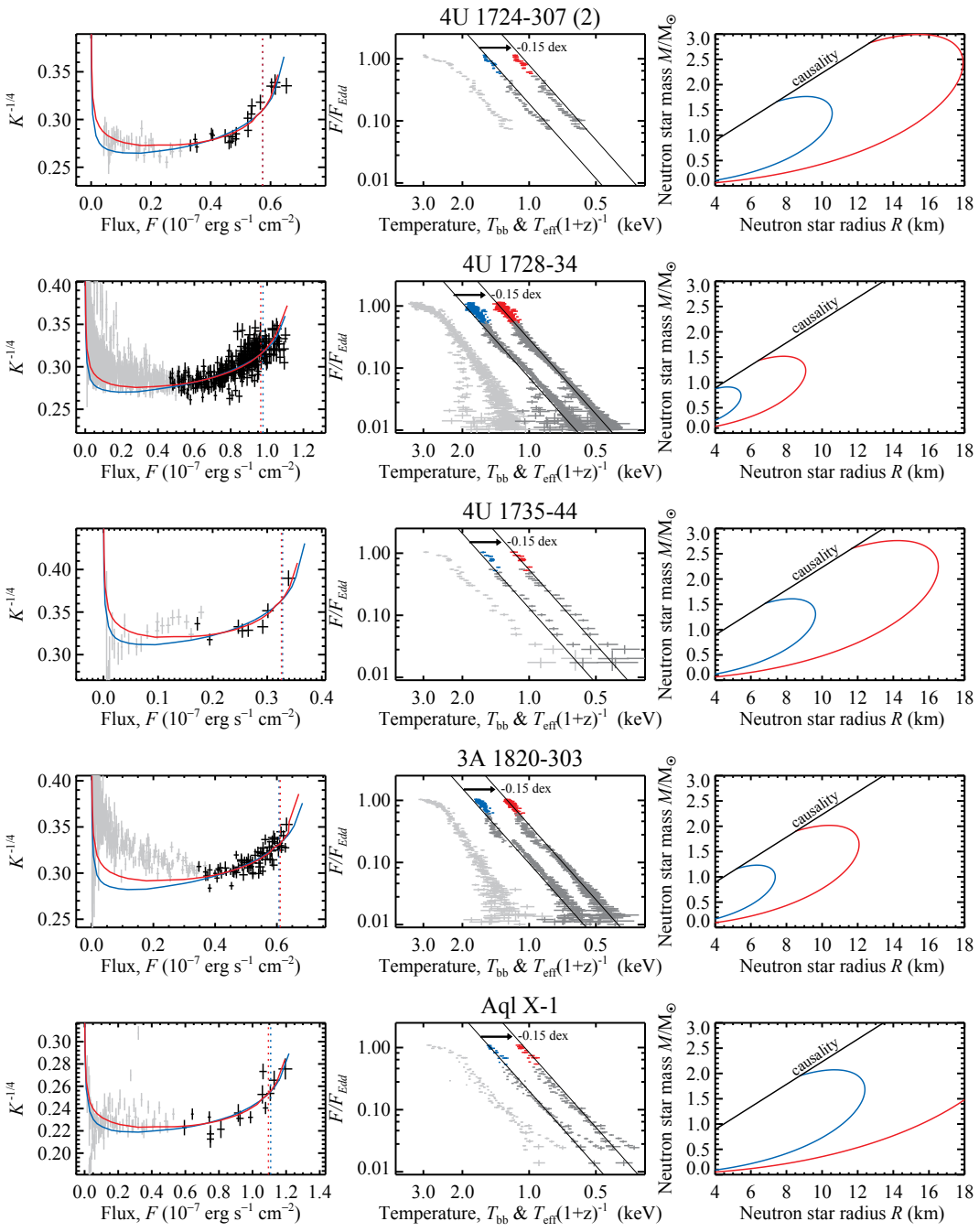

Figure 5.1: (Continued from the previous page.) The straight inclined lines show a powerlaw with an index of 4 corresponding to the $L \propto T^4$ relation. For clarity, the temperatures corresponding to the helium models are shifted by -0.15 dex to the right. The last column of figures shows the $M - R$ relation for the constant Eddington temperature $T_{\rm Edd}$. Hydrogen atmosphere models are represented with blue and helium atmospheres with red lines.

Taking a distribution of distances (see Chapter 2.1), we then convert a distribution of A and $F_{\rm Edd}$ using Monte-Carlo simulations to the distribution of M and R. The resulting contours are elongated because of the uncertainty in the distance, along the curves of the constant Eddington temperature (see the third column of Figure 5.1 and Figure 5.3).

Chemical composition

When comparing the mass and radius results from the Eddington temperatures, we are able to deduce the chemical composition for each of the sources (see Table 5.1) by considering only the physically motivated results. In many cases one chemical composition points out to a mass between $1-2M_{\odot}$ and a radius between $10-15$ km while another gives unrealistic results of $R > 20$ km and/or $M > 3M_{\odot}$ (see third column of Figure 5.1).

The chemical compositions obtained seem to be evenly distributed between the hydrogen and helium compositions. Many of these are also well supported by other kinds of observations and methods (see e.g. Galloway et al. 2008).

Constraints on the equation of state

By fixing the chemical composition, we can analyse the distribution of masses and radii. For 4U 1728–34 we get a very small radius compared to the others while the cooling tail has a very large scatter (See Figure 5.1). This could originate because the accretion disc around the star could, in some cases, reflect the outgoing radiation. Due to uncertainties arising from this, we neglect this source from further analysis.

After this source is neglected, we obtain consistent results from the chosen set of LMXB sources with the fixed chemical compositions. Because the distances are unknown for many sources, we obtain a large range of masses. Due to this, we set some strict mass limits for the sources that do not reside in any known globular cluster. A rather conservative lower limit of $M > 1.1M_{\odot}$ is chosen based on the fall-back simulations by Zhang et al. (2008) with the smallest mass of $M_{\rm min} = 1.08M_{\odot}$ produced in their simulations. The upper limit is set to be at $M < 2.2M_{\odot}$. Based on these lower and upper limit cutoffs we can neglect some effects of the freely varying distance distributions.

The obtained mass and radius constraints are shown separately for all of the sources in Table 5.1. A better way, however, is to consider the contours directly in the $M-R$ plane, because results are elongated along the constant Eddington temperature (see Figure 5.3).

Table 5.1: Results for sources with hard RE bursts

Source	$F_{\rm Edd}$[a]	A[b]	Mass[c]	Radius[d]	Comp.[e]
4U 1608–52	1.107	0.135	1.85	$17.05^{+0.54\ (+0.78)}_{-1.78\ (-2.60)}$	H
4U 1636–536 (1)	0.529	0.192	1.18	$16.50^{+0.81\ (+1.91)}_{-1.23\ (-2.05)}$	He
4U 1636–536 (2)	0.662	0.189	1.24	$14.86^{+0.28\ (+1.23)}_{-1.23\ (-1.77)}$	He
4U 1702–429	0.771	0.189	1.30	$13.22^{+0.42\ (+0.43)}_{-0.54\ (-1.08)}$	He
4U 1724–307 (1)	0.584	0.152	$1.88^{+0.16\ (+0.18)}_{-0.17\ (-0.21)}$	$19.44_{-2.58\ (-3.09)}$[f]	H
4U 1724–307 (2)	0.575	0.173	$1.91^{+0.12\ (+0.24)}_{-0.20\ (-0.46)}$	$12.82^{+0.95\ (+2.04)}_{-0.24\ (-0.96)}$	H
			$2.12^{+0.15\ (+0.33)}_{-0.06\ (-0.15)}$	$10.50^{+1.23\ (+1.91)}_{-0.41\ (-1.37)}$	
4U 1735–44	0.326	0.222	1.29	$16.63^{+1.09\ (+1.64)}_{-0.95\ (-1.77)}$	He
3A 1820–303	0.611	0.206	$1.82^{+0.12\ (+0.18)}_{-0.15\ (-0.34)}$	$12.13^{+0.69\ (+1.77)}_{-0.13\ (-0.68)}$	He
			$2.00^{+0.09\ (+0.24)}_{-0.04\ (-0.09)}$	$11.05^{+0.45\ (+0.67)}_{-1.10\ (-2.05)}$	
Aql X-1	1.000	0.140	1.36	$17.45^{+0.41\ (+0.55)}_{-1.77\ (-2.86)}$	H
All sources			$1.87^{+0.19\ (0.31)}_{-0.36\ (-0.66)}$	$12.68^{+4.64\ (+5.05)}_{-0.68\ (-1.09)}$	
			$2.15^{+0.01\ (0.03)}_{-0.15\ (-0.19)}$	$10.50^{+0.55\ (+1.64)}_{-0.82\ (-1.36)}$	

[a] Best-fit Eddington flux in units of 10^{-7} erg cm^{-2} s^{-1}.

[b] Best-fit normalization in units of (km/10 kpc)$^{-1/2}$.

[c] Neutron star mass in units of $M_\odot$ where the main errors correspond to 1σ confidence levels. Errors corresponding to a 2σ confidence level are enclosed in parentheses. Note that in many cases, due to unknown distance, the masses are distributed between our chosen interval of $1.1 - 2.2 M_\odot$. In these cases we only give the most probable value.

[d] Neutron star radius in units of km. Same error notation as with the mass is being used.

[e] Chemical composition of the atmosphere.

[f] Only the lower limit for the radius is given because the distribution of the radius extends to over 20 km.

Note that in the case of 4U 1636–536 and 4U 1724–307 we present the results for two different cooling tracks. For 4U 1724–307 (2), 3A 1820–303 and for the combined results, a second physically realistic solution exists that is presented directly after the first set of results.

After combining the results from all of the sources, we obtain two physically realistic solutions for the mass and radius (see Table 5.1). The statistically more probable solution gives the mean neutron star radius to be around 12.7 km for a mean mass of 1.87 $M_{\odot}$. The lower limit for the radius, in this case, is 11.6 km for a 2σ confidence level. The mass and radius distributions from Monte Carlo simulations also indicate another solution with a probability of 40% compared to our first solution with a mean radius of 10.5 km for a mass between $2.0 - 2.2$ $M_{\odot}$ (2σ confidence level). In this case the lower limit for the radius is around 9.1 km, again for a 2σ confidence level. For the combined contours, see Figure 5.2.

These are important measurements, as they rule out the exotic equations of states of matter inside neutron stars (for e.g. SQM3 in Figure 5.2). These soft equations of states of matter rely on an assumption that the inner core is made of the strange quark matter. However, according to our results, this seems not to be the case as our constraints point out to stiff equations of states. This implies that the core is, in fact, mostly made of pure neutrons. This is also supported by some newly made discoveries of heavy neutron stars with a mass of around $2M_{\odot}$ (see e.g. Demorest et al. 2010; Antoniadis et al. 2013) that can not be produced by the strange quark matter only.

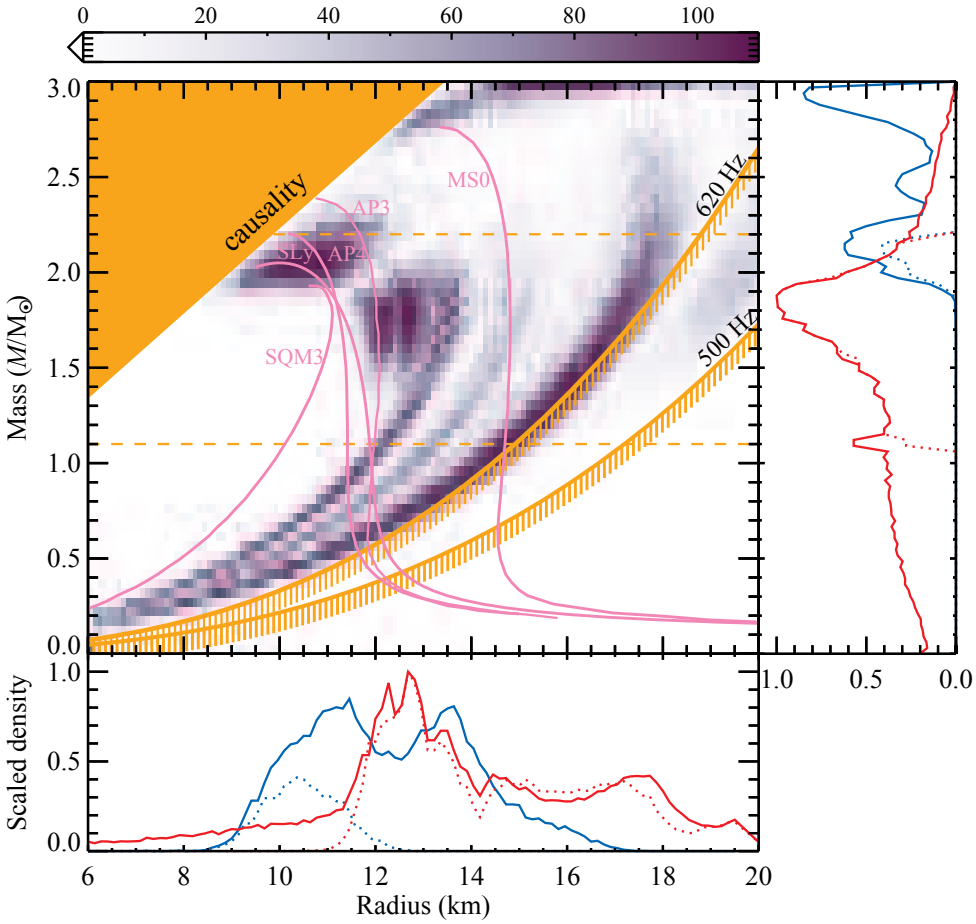

Figure 5.2: Combined results for hydrogen and helium atmospheres. The mass-radius relation for several equations of state of neutron star and strange star matter are shown by pink curves (Haensel et al., 2007). The upper-left region is excluded by constraints from the causality requirements (Haensel et al., 2007; Lattimer & Prakash, 2007). The lower panel of figure shows the scaled density of the radius points and the right panel that of the mass points. The red and blue lines correspond to different sets of solutions. The dotted lines show the same distributions when the mass is limited between $1.1M_{\odot} < M < 2.2M_{\odot}$. Note that the distributions of the two sets of solutions are also scaled between each other by the probability to obtain each result.

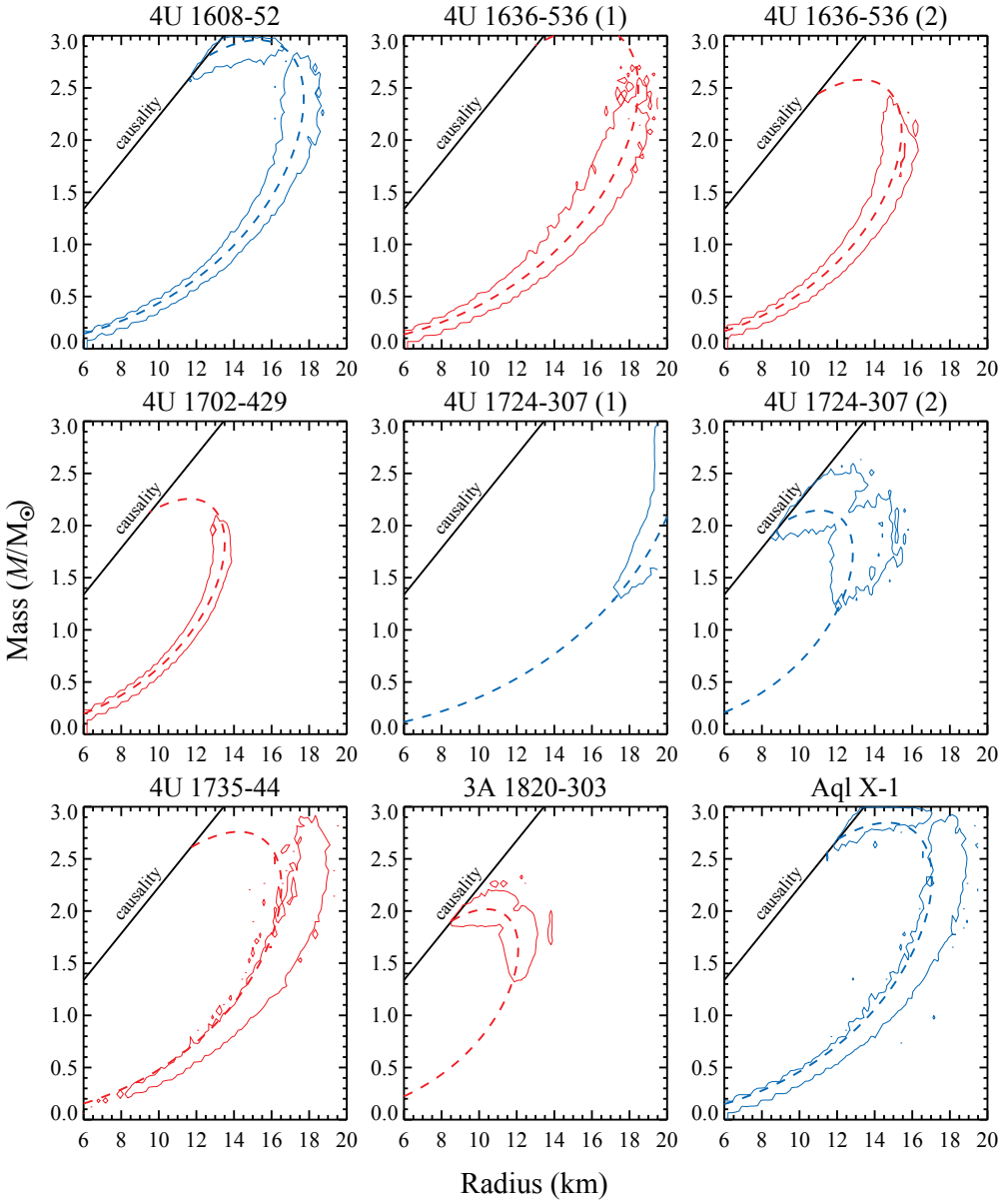

Figure 5.3: Mass and radius constraints for different sources. The contours show the 95% confidence level and the dashed line the constant Eddington temperature corresponding to the best fit value. For clarity, pure hydrogen atmospheres are marked with blue lines and helium atmospheres with red lines.

Chapter 6

Summary and conclusions

In the first chapter of this thesis, we discussed the physics behind the neutron star X-ray bursts. We introduced the mechanism of the burst ignition and compared the differences between different chemical compositions. We also classified the bursts based on these properties and showed that there exists an energetic subclass of bursts that show expansion of the whole photosphere of the star. These PRE bursts were then analysed more closely in order to constrain the mass and radii of the neutron stars.

Data reduction and the concerning tasks for analysing the *RXTE*/PCA data were then presented. We also introduced our set of bursting LMXB systems that we use in the mass and radius determination. Finally, we formulated a set of selection rules for choosing the PRE bursts from all the observed bursts present in our catalogue.

After this, we presented the basic framework for the calculation of the neutron star atmosphere models. We used the results from these models to derive a connection between the theoretical and observed cooldown of the PRE bursts. A small correction to this cooling tail method was also introduced by replacing the previously used approximative relation $f_{\rm c} - l$ by $w^{-1/4} - w f_{\rm c}^4 l$.

Due to the influence of the accretion flow on the cooling of the atmospheres, we need to separate between bursts occuring at high and low accretion rates. Methods and criteria for this were given in the fourth chapter. There we showed that only the hard state bursts should be used with the cooling tail method.

Finally, the main results of this research were presented in the fifth chapter. We constrained the neutron star radius to most likely be around $12 - 16$ km for a mass of around $1.8 M_{\odot}$. This implies a stiff equation of state of the

matter inside neutron stars. We also deduced the chemical composition of the atmosphere for each of the sources by choosing only the physically motivated results. These compositions are supported by other kinds of measurements and can be used as a validation when making more precise constraints in the future.

Our methods still contain some sources of systematic errors that we plan to address in the future work. The most important of these is the rotation of the neutron star that is not yet taken into account. Due to a fast rotation, the neutron star is actually not spherical as was assumed here. Effects from the Doppler shift could also distort the observed spectrum. By solving these issues in the future work, we then hope to constrain the mass and radius with such an accuracy that the equation of state of the matter inside neutron stars can finally be pinpointed.

Bibliography

Aharonian F. A., Atoyan A. M., 1981, Ap&SS, 79, 321

Antoniadis J. et al., 2013, Science, 340, 448

Arnaud K. A., 1996, in ASP Conf. Ser. 101, Astronomical Data Analysis Software and Systems V, ed. Jacoby G. H., Barnes J. (San Francisco: ASP), 17

Belian R. D., Conner J. P., Evans W. D., 1976, ApJ, 206, L135

Bradt H. V., Rothschild R. E., Swank J. H., 1993, A&AS, 97, 355

Carrier F., Barblan F., Burki G., Bartholdi P., Nicolet B., 2003, A&A, 398, 1073

Churazov E., Gilfanov M., Forman W., Jones C., 1996, ApJ, 471, 673

Demorest P. B., Pennucci T., Ransom S. M., Roberts M. S. E., Hessels J. W. T., 2010, Nature, 467, 1081

Done C., Gierliński M., Kubota A., 2007, A&A Rev., 15, 1

Ebisuzaki T., 1987, PASJ, 39, 287

Fowler W. A., Hoyle F., 1965, Nucleosynthesis in massive stars and supernovae (Chicago: University of Chicago Press)

Frank J., King A., Raine D. J., 2002, Accretion Power in Astrophysics (Cambridge: Cambridge University Press)

Galloway D. K., Muno M. P., Hartman J. M., Psaltis D., Chakrabarty D., 2008, ApJS, 179, 360

Gilfanov M., Churazov E., Revnivtsev M., 1999, A&A, 352, 182

Gilfanov M., Revnivtsev M., Molkov S., 2003, A&A, 410, 217

Grindlay J. et al., 1976, ApJ, 205, L127

Gruber D. E. et al., 1996, A&AS, 120, C641

Haensel P., Potekhin A. Y., Yakovlev D. G., 2007, Astrophysics and Space Science Library, Vol. 326, Neutron Stars 1: Equation of State and Structure (New York: Springer)

Hansen C. J., van Horn H. M., 1975, ApJ, 195, 735

Hasinger G., van der Klis M., 1989, A&A, 225, 79

Hubeny I., Hummer D. G., Lanz T., 1994, A&A, 282, 151

Hummer D. G., Mihalas D., 1988, ApJ, 331, 794

Jahoda K. et al., 2006, ApJS, 163, 401

Kuulkers E. et al., 2003, A&A, 399, 663

Lattimer J. M., Prakash M., 2001, ApJ, 550, 426

Lattimer J. M., Prakash M., 2004, Sci, 304, 536

Lattimer J. M., Prakash M., 2007, Phys. Rep., 442, 109

Lattimer J. M., Prakash M., Masak D., Yahil A., 1990, ApJ, 355, 241

Latvala O.-M., 2012, Master's thesis (Oulu: University of Oulu)

Levine A. M. et al., 1996, ApJ, 469, L33

Lewin W. H. G., Vacca W. D., Basinska E. M., 1984, ApJ, 277, L57

Lewin W. H. G., van Paradijs J., Taam R. E., 1993, Space Science Reviews, 62, 223

London R. A., Howard W. M., Taam R. E., 1984, ApJ, 287, L27

London R. A., Taam R. E., Howard W. M., 1986, ApJ, 306, 170

Madej J., 1991, ApJ, 376, 161

Muno M. P., Remillard R. A., Chakrabarty D., 2002, ApJ, 568, L35

Nagirner D. I., Poutanen J., 1994, Astrophys. Space Phys. Rev., 9, 1

Oppenheimer J. R., Volkoff G. M., 1939, Physical Review, 55, 374

Pavlov G. G., Shibanov I. A., Zavlin V. E., 1991, MNRAS, 253, 193

Pedersen H., van Paradijs J., Lewin W. H. G., 1981, Nature, 294, 725

Penninx W., Damen E., van Paradijs J., Tan J., Lewin W. H. G., 1989, A&A, 208, 146

Poutanen J., Svensson R., 1996, ApJ, 470, 249

Prasad M. K., Kershaw D. S., Beason J. D., 1986, Appl. Phys. Lett., 48, 1193

Steiner A. W., Lattimer J. M., Brown E. F., 2010, ApJ, 722, 33

Strohmayer T., Bildsten L., 2006, Cambridge Astrophysics Series 39, Compact stellar X-ray sources, ed. Lewin W., van der Klis M., (Cambridge: Cambridge University Press), 113

Suleimanov V., Poutanen J., 2006, MNRAS, 369, 2036

Suleimanov V., Poutanen J., Revnivtsev M., Werner K., 2011a, ApJ, 742, 122

Suleimanov V., Poutanen J., Werner K., 2011b, A&A, 527, A139

Suleimanov V., Poutanen J., Werner K., 2012, A&A, 545, A120

Tawara Y., Hayakawa S., Kii T., 1984, PASJ, 36, 845

Thorstensen J., Charles P., Bowyer S., 1978, ApJ, 220, L131

Tolman R. C., 1934, Proceedings of the National Academy of Science, 20, 169

van Paradijs J., 1978, Nature, 274, 650

van Paradijs J., Dotani T., Tanaka Y., Tsuru T., 1990, PASJ, 42, 633

van Paradijs J., Lewin W. H. G., 1987, A&A, 172, L20

van Paradijs J., Verbunt F., van der Linden T., Pedersen H., Wamsteker W., 1980, ApJ, 241, L161

Vrtilek S. D. et al., 1990, A&A, 235, 162

Zavlin V. E., Pavlov G. G., Shibanov Y. A., 1996, A&A, 315, 141

Zavlin V. E., Shibanov Y. A., 1991, Sov. Astr., 35, 499

Zhang W., Woosley S. E., Heger A., 2008, ApJ, 679, 639